J. Fluid Mech. (2019), *vol.* 858, *pp.* 714–759.
doi:10.1017/jfm.2018.809

Numerical investigation of laminar–turbulent transition in laminar separation bubbles: the effect of free-stream turbulence

Shirzad Hosseinverdi[1,†] **and Hermann F. Fasel**[1]

[1]Department of Aerospace and Mechanical Engineering, University of Arizona, Tucson, AZ 85721, USA

(Received 14 September 2017; revised 1 October 2018; accepted 8 October 2018)

The role of free-stream turbulence (FST) in the hydrodynamic instability mechanisms and transition to turbulence in laminar separation bubbles (LSBs) was investigated using direct numerical simulations (DNS). Towards this end, a set of highly resolved DNS have been carried out, where isotropic FST fluctuations with intensities from 0.1 % to 3 % are introduced to investigate the relevant physical mechanisms governing the interaction of separation and transition in LSBs. For disturbance-free simulations, i.e. without FST, laminar–turbulent transition involves a Kelvin–Helmholtz (KH) instability of the separated shear layer. For LSBs subjected to FST, vortical FST fluctuations penetrate the approaching attached laminar boundary layer upstream of the separation location and induce slowly growing low-frequency disturbances, so-called Klebanoff (K) modes, which cause a spanwise modulation with a distinct spanwise wavelength. Simultaneously, the FST enhances the initial levels of instability waves with frequencies in the frequency range of the KH instability, but at much smaller amplitude levels compared to the K-modes. Results from the calculations based on the linearized Navier–Stokes equations and comparison with DNS results reveal that the K-mode exhibits exponential growth in the separated shear layer until it reaches a peak amplitude. At the same time, two-dimensional (2D) disturbance waves are also exponentially amplified, in fact at larger growth rate compared to the K-mode, due to the primary (convective) shear-layer instability mechanism until they saturate downstream of the peak amplitude associated with the K-mode. Therefore, based on detailed spectral analysis and modal decompositions for the separation bubbles investigated, the transition process is the result of two different mechanisms: (i) strong amplification of high-frequency (order of the shedding frequency), essentially 2D or weakly oblique fluctuating disturbances and (ii) low-frequency, three-dimensional K-modes caused by FST. Depending on the intensity of the FST, one of these mechanisms would dominate the transition process, or both mechanisms act together and contribute simultaneously. The net effect of these two events is an acceleration of transition for an increased level of FST intensity, which in turn leads to a reduction of the extent of the separation bubble in streamwise and wall-normal directions. The ‘roll-up’ into spanwise large-scale vortical structures resulting from the shear-layer instability, and the eventual breakdown of these structures, strongly contribute to the reattachment process. The spanwise coherence of these ‘rollers’ deteriorates due to

† Email address for correspondence: shirzadh@email.arizona.edu

the presence of large-amplitude K-modes, thus effectively weakening their strength for high levels of FST intensities ($Tu > 1\,\%$).

Key words: boundary layer separation, instability, transition to turbulence

1. Introduction

When subjected to a strong enough adverse pressure gradient, a laminar boundary layer detaches from the wall. For sufficiently large Reynolds numbers, the separated shear layer will transition in the separated region and lead to turbulent reattachment, thus creating a so-called laminar separation bubble (Horton 1968; Gaster 1969). Laminar separation bubbles (LSBs) are encountered in many important aeronautical applications, such as wings of unmanned aerial vehicles, multi-element airfoil configurations, low-pressure turbine blades to name a few. Owing to the small characteristic length scale of some of these components or the fact that they are operated at large altitudes where the air density is low, the operating Reynolds number can drop to low values ($Re < 10^5$). For such low Reynolds numbers, boundary layers can remain laminar and therefore are highly susceptible to separation and the generation of LSBs. Separation is associated with several undesirable effects. Large separation bubbles can drastically reduce the aerodynamic efficiency by reducing the usable lift and increasing drag. Another aspect is the increase in unsteadiness and noise caused by the flow separation.

Depending on the governing parameters such as Reynolds number, pressure gradient and external disturbances such as free-stream turbulence (FST), LSBs can be classified as either ‘short’ or ‘long’. There are several parameters suggested by researchers to classify whether a bubble is ‘short’ or ‘long’ – see, for example, Owen & Klanfer (1953), Gaster (1969) and Diwan, Chetan & Ramesh (2006). An intuitive way to define a bubble as either ‘short’ or ‘long’ is based on assessing their effect on the pressure distribution. Towards this end, if the effect of a separation bubble on the pressure distribution is local and limited, it is a ‘short’ bubble; while a ‘long’ bubble has a strong upstream and downstream impact on the inviscid pressure field.

The separated shear layer in LSBs is highly unstable with respect to small disturbances within the flow, thus allowing for rapid growth of vortical structures. These structures will have an effect on the separation and reattachment behaviour and therefore significantly affect the size and the shape of the separated region (or separation bubble). Thus, the instabilities and the laminar–turbulent transition process have a profound impact on the mean flow topology and the unsteady behaviour of LSBs (Dovgal, Kozlov & Michalke 1994; Boiko *et al.* 2002). Therefore, an improved understanding of the relevant physical mechanisms governing separation in general and the transition process in particular is required. This may lead to useful separation prediction tools that include the effects of the unsteady behaviour. This in turn could enable the development of novel geometries with more favourable hydrodynamic or aerodynamic properties. This understanding may also reveal possibilities for novel active/passive flow control strategies that may help prevent (or at least mitigate) the negative effects of separation.

1.1. *Basic characteristics of hydrodynamic instability in a laminar separation bubble*

For a zero-pressure-gradient flat-plate boundary layer and a low-amplitude disturbance environment, transition can be initiated by the exponential growth of so-called Tollmien–Schlichting (TS) waves when the critical Reynolds number Re_{cr} is exceeded, whereby the environmental disturbances enter the boundary layer via a so-called 'receptivity' mechanism (Morkovin 1969). An adverse pressure gradient (APG) has a destabilizing effect, effectively decreasing the critical Reynolds number. If the APG is strong enough, the flow separates: the resulting velocity profile in the separated region becomes inviscidly unstable (Kelvin–Helmholtz (KH) instability), due to the presence of an inflection point in the velocity profile. This leads to growth rates of the instability waves that are much larger compared to the growth rates associated with TS instabilities for an attached boundary layer. Generally, larger distances between the shear layer and the wall lead to larger spatial amplification rates with a small Reynolds-number dependence (see Rist & Maucher 2002). Separated shear layers are unstable to a broad band of spanwise wavenumbers and frequencies and usually high-frequency, two-dimensional (2D), or weakly oblique disturbances can rapidly reach large (nonlinear) amplitudes within the separated region, leading to the commonly observed periodic shedding of spanwise coherent vortical structures (Rist 2003). At this stage, secondary instabilities could take hold, which will subsequently lead to a rapid breakdown to small-scale three-dimensional (3D) structures and eventually to a fully turbulent flow. While the separated regions allow for a rapid growth of vortical disturbance waves, at the same time the presence of the large-amplitude waves (or vortices) facilitates an exchange of momentum, which limits the extent and intensity of the separation. Consequently, separation and transition are intricately linked.

A number of detailed investigations (experimental and numerical) have addressed laminar–turbulent transition in LSBs in the framework of spatially growing perturbations, i.e. a convective amplification of 2D or weakly oblique fluctuating disturbances. In a direct numerical simulation (DNS) of a separation bubble conducted by Alam & Sandham (2000), controlled periodic 3D disturbance waves with a fixed frequency and wavenumber were introduced upstream of the separation, and the evolution of the disturbances was then tracked all the way to the reattachment region. They concluded that the separated shear layer undergoes transition via oblique modes and staggered Λ-vortices are observed in the flow prior to breakdown. A combined experimental/numerical investigation was carried by Marxen *et al.* (2003) using controlled disturbance input. They found that transition in the 2D LSB is driven by a convective primary amplification of 2D disturbance waves, resulting into spanwise rollers that are shed from the separation bubble. It is worth noting that, inside the LSB, 2D disturbance waves are the most amplified. However, weakly oblique disturbances (3D modes with small wave angles) can also experience strong amplification rates that are close to those of the 2D modes (Marxen *et al.* 2003; Marxen, Rist & Wagner 2004). Thus, the initial amplitudes resulting from the receptivity process will dictate which disturbance modes prevail downstream of the separation location and thus dominate the transition process.

Following the work of Gaster & Grant (1975), who were the first to use localized ('point') pulse disturbances to generate wave packets in a zero-pressure-gradient flat-plate boundary layer, Watmuff (1999) carried out a detailed experimental study of 2D LSBs (using the pulse disturbance technique of Gaster & Grant 1975) in an effort to understand the underlying instability mechanism in the separated flow. He concluded that the primary instability is an inviscid inflectional mechanism typical of a KH

instability. The localized (point) pulse disturbance method was subsequently used by Diwan & Ramesh (2009), who carried out an experimental study of an LSB and the associated linear stability mechanisms. In contrast to the traditional view that connects the origin of the inviscid instability in a bubble to the separated shear layer outside the bubble and its KH mechanism, Diwan & Ramesh (2009) provided evidence that the origin of the inflectional instability can be traced back to the region upstream of the separation bubble where TS waves are generated (by the receptivity) and amplified due to a viscous instability in the attached APG region of the boundary layer.

Instead of spanwise-localized pulse disturbances as in Gaster & Grant (1975), Michelis, Yarusevych & Kotsonis (2017) investigated the spatial and temporal response of an LSB to 2D (spanwise-uniform) pulse disturbances by means of time-resolved particle image velocimetry. The pulse disturbances develop into wave packets that lead to a rapid shortening of the bubble due to later separation and earlier reattachment compared to the unforced case. This process is followed by a so-called 'bubble bursting', during which the bubble grows significantly in size, while the shedding of spanwise vortical structures is halted. Using linear stability analysis based on the phase-averaged flow field, they showed that amplification rates are directly proportional to the shape factor throughout the recovery of the bubble to its unforced state. This was important since it indicates that bursting and flapping (intermittent shear-layer fluctuation) mechanisms are driven by the altered stability characteristics due to the variation in incoming disturbances.

A weak concave streamline curvature occurs near the separation location of an LSB which may give rise to a Görtler instability despite the absence of a curved surface. This instability may be a candidate for explaining the appearance of steady 3D disturbances, as examined by Marxen *et al.* (2009). Based on a qualitatively good correlation of the growth rate and an equivalent Görtler number (G_{eq}), as well as on the shape of the amplitude functions, they showed that the onset of the instability is due to streamline curvature, i.e. due to a Görtler-type instability. The streamwise disturbance development was explained by two different mechanisms: spatial transient growth and a modal Görtler-type instability. In certain parts of the domain, the two effects are blended and contribute simultaneously to the disturbance shape. In both mechanisms, the lift-up effect feeds the growth of the streamwise velocity component. It is important to note that a Görtler -type instability can only be expected in LSBs in the part of the flow further away from the wall where G_{eq} possesses appreciable values. In the work by Marxen *et al.* (2009), G_{eq} is approximately 5 near the separation location.

Evidence for self-sustained transition to turbulence without external forcing is presented by Spalart & Strelets (2000) and Jones, Sandberg & Sandham (2008). The sustaining of turbulence without external disturbances cannot be explained by the convective instability mechanics. Convective instability refers to the downstream amplifications of small-amplitude disturbance waves, which were generated at some location upstream. Without a constant disturbance input, the disturbance waves will eventually decay completely and transition to turbulence will not occur. The onset of unsteadiness in LSBs may be attributed to the absolute instability mechanism (Huerre & Monkewitz 1990) where the disturbance waves propagate in both the downstream and upstream directions while being amplified in time, independent of external excitations and ultimately would result in transition. There are several numerical and theoretical studies conducted addressing absolute instability in LSBs (Hammond & Redekopp 1998; Hosseinverdi & Fasel 2013*a*; Rodríguez, Gennaro & Juniper 2013; Embacher & Fasel 2014). For a separation bubble, two parameters play an important

role in the context of absolute instability: (i) the height of the bubble and (ii) the magnitude of the reverse flow. In general, a reverse flow of approximately 7 %–10 % of the free-stream velocity in the bubble is required for the onset of an absolute instability (Rodríguez & Theofilis 2010). The typical frequency of this instability is very low, and the most amplified mode is stationary with a spanwise length scale of the order of the streamwise extent of the vortex containing the trapped flow inside the separation bubble. Rodríguez *et al.* (2013) demonstrated that the nature of such an instability mode is a global centrifugal instability, which requires a reverse flow with a magnitude of 7 %–8 % of the free-stream velocity.

1.2. *The influence of free-stream turbulence*

Almost all of the above transition investigations only address the so-called 'controlled transition scenarios', which may be observed only in carefully controlled water/wind tunnel experiments where the environmental disturbances, such as FST, noise and vibration, have been reduced to a minimum. Therefore, the question arises whether this path to turbulence is still prevalent in a 'real' environment such as encountered in free flight, for example. Considering technical applications, it is reasonable to assume that the most general disturbances inducing laminar–turbulent transition are due to FST. As mentioned above, the behaviour of LSBs strongly depends on the transition process within the shear layer, and for this reason one would expect that the FST plays an important role governing the extent and unsteady characteristic of the bubble. Thus, FST has to be considered when investigating laminar–turbulent transition in LSBs for practical applications.

Numerous experimental, theoretical and numerical investigations have addressed the role of FST on laminar–turbulent transition in a boundary layer. In the absence of pressure-gradient effects, for attached boundary layers with imposed FST, transition appears to be preceded by streamwise 'streaks' in the boundary layer. These streaks are caused by 'Klebanoff modes' (K-modes), after P. S. Klebanoff who first identified them (Klebanoff & Tidstrom 1959; Klebanoff 1971). His findings have been confirmed in numerous experiments and numerical simulations by other researchers (Kendall 1985, 1990; Westin *et al.* 1994; Leib, Wundrow & Goldstein 1999; Jacobs & Durbin 2001; Fasel 2002; Brandt, Schlatter & Henningson 2004; Goldstein 2014). The streamwise streaks caused by FST correspond to a thinning and thickening of the boundary layer. The K-mode leads to a significant distortion in the form of the u-velocity component in the spanwise and wall-normal directions. K-modes are fundamentally different from TS waves. Characteristic features of the K-mode are its low frequency, low growth rate and spanwise length scale of a few boundary-layer thicknesses.

The growth of the disturbances, algebraic instead of exponential, was explained by the lift-up mechanism (Landahl 1975). A physical explanation for this growth is that streamwise perturbations can be generated by the lifting-up of fluid particles in the presence of a mean shear layer. The strong response of the boundary layer to the narrow band of the wavenumber–frequency spectrum is explained by the viscous theory that the boundary layer acts as a low-pass filter, admitting long-wavelength, low-frequency, free-stream disturbances. Low-frequency vortical disturbances caused by FST are more unstable in the presence of an APG, resulting in stronger Klebanoff distortions, and hence provoke early transition (Zaki & Durbin 2006). In boundary layers with FST intensities of 1 % or more, transition occurs rapidly, bypassing the natural transition scenario (Morkovin 1969; Kendall 1985; Jacobs & Durbin 2001).

The effect of FST on the transition in LSBs has not been addressed as extensively/detailed as for attached laminar boundary layers. Häggmark (2000) provided some experimental results on the effects of FST on LSBs induced by an APG. FST with an intensity of 1.5 % was generated by a grid upstream of the leading edge of the plate. No strong evidence for the existence of 2D waves, which are typical for separation bubbles in an undisturbed environment, could be produced. On other hand, the existence of low-frequency streaky structures in the boundary layer upstream of separation and in the separated boundary layer was revealed by smoke visualization photographs and spectral analysis.

One of the first preliminary numerical investigations into the effects of FST on transitional LSBs was DNS by Wissink & Rodi (2006) where a 2D LSB was formed on a flat plate due to a strong APG imposed by a contoured wall mounted at a distance above the flat plate. The free-stream disturbances with 5 % intensity were obtained by a separate large-eddy simulation (LES) of isotropic turbulence and added at the inflow boundary for the DNS. It is worth noting that the inflow boundary was placed upstream of the leading edge of the flat plate. Because of the strong downstream decay, the level of FST was much lower at the leading edge (approximately 1.5 %). With oncoming FST fluctuations, the KH instability was triggered much earlier and transition was enhanced, leading to a drastic reduction in the size of the separation bubble. Using a simulation set-up similar to Wissink & Rodi (2006), Lardeau, Leschziner & Zaki (2012) carried out LES of 2D LSBs subjected to different levels of FST intensity, ranging from 0 to 2 % at the separation location. Consistent with Wissink & Rodi (2006), elongated streamwise structures (K-modes) prior to the separation location led to a faster breakdown of the KH vortices. They concluded that the energy carried by the Klebanoff modes increases with the FST intensity, and thus leads to a greater reduction in the mean separated region. It is important to note that the investigation of Lardeau *et al.* (2012) indicated a significant influence of the subgrid-scale modelling on the mean flow and turbulence statistics of the LES results for the cases with FST. Another LES of pressure-induced separation bubbles exposed to FST fluctuations was performed by Rao *et al.* (2013). However, the inflow condition was generated by combining the incoming FST with wakes superimposed onto the mean velocity profile. Confirming the previous numerical and experimental investigations with respect to the role of FST, they showed that stronger Klebanoff modes are formed in the presence of wakes when compared to the streaks due to FST alone.

For ‘short’ LSBs, a numerical investigation by McAuliffe & Yaras (2010) showed that the nature of the instability mechanisms changes from amplification due to the KH instability to amplification of streamwise streaks for elevated levels of FST (FST intensity of 1.45 % at separation location). These streaks extend into the region of the laminar separated flow and initiate breakdown via the formation of turbulent spots. Brinkerhoff & Yaras (2015) performed DNS of an attached boundary layer subjected to streamwise pressure gradients and high FST intensity (5.3 % at the leading edge). They found that a favourable pressure gradient stabilized longitudinal streamwise streaks caused by FST in the laminar boundary layer until further downstream in the APG region where transition to turbulence was triggered via the development of a varicose secondary instability of individual low-speed streaks, which led to the breakdown to turbulence. The laminar–turbulent transition process was also linked to a rapid amplification of free-stream disturbances in the inflectional boundary layer in the APG region that resulted in a largely homogeneous breakdown to turbulence across the spanwise direction.

In detailed numerical simulations of a separation bubble forming over a flat plate subject to FST, Balzer & Fasel (2016) showed that even very small FST levels caused a significant reduction of the size of the separation bubble, indicating a strong effect of FST on transitional LSBs. Elevated FST levels led to the generation of low-frequency disturbances with distinct spanwise spacing inside the boundary layer (K-modes). Consistent with the previous numerical and experimental investigations, increasing the FST levels led to accelerated transition and a reduction of the (average) bubble size. Of particular interest was the observation that the inviscid shear-layer instability was present even for high FST intensity of 2.5 % and was not 'bypassed'. Thus, they concluded that the transition to turbulence was a consequence of both the primary shear-layer instability and the enhanced 3D disturbance level, in particular the streamwise streaks caused by the FST. DNS of transitional flow in a linear compressor passage at high levels of FST intensities (from 3.25 % up to 10 %) by Zaki *et al.* (2010) revealed that high levels of FST can even prevent separation completely by transitioning the flow upstream of the separation location.

The acceleration of transition and the shrinking of the separated region for elevated levels of FST have also been reported in experimental studies by Burgmann & Schröder (2008) and Olson *et al.* (2013) for the flow over a SD7003 airfoil, and by Simoni *et al.* (2017) for LSBs forming on a flat plate. The work by Olson *et al.* (2013) exhibited strong sensitivity of transitional LSBs to FST level, which makes it very difficult to compare results obtained in different experimental facilities and with the experimental and computational results as well. Furthermore, Simoni *et al.* (2017) identified that the dependence of the mean characteristics of LSBs on the level of FST is different for different Reynolds numbers. They conjectured that the Reynolds-number variation mainly drives the length scale associated with the KH vortices whereas increasing the intensity of FST level shifts the onset of the shedding phenomenon upstream. An interesting observation from the work by Burgmann & Schröder (2008) was that the shedding frequencies associated with KH vortices are more or less unaffected by the turbulence intensity; they speculated that the earlier transition does not seem to affect the vortex roll-up process itself, but rather only the size of the vortices.

In the overview above of the numerical and experimental investigations of LSBs with respect to the role of FST, emphasis has been mainly on first- and second-order statistics (time average and turbulence statistics). Experimental measurements have been carried out mainly in an x–y plane (suitable for investigating KH instability), and thus missing the 3D nature of instability waves caused by FST. On the other hand, 3D numerical simulations mostly focused on the existence of streamwise streaks (K-modes) caused by FST, mainly using instantaneous flow visualizations (e.g. u-velocity or Q-criterion). However, the streamwise evolution of such instability modes and their interaction with other instability mechanisms acting on the LSB (for example, KH) have not been investigated in detail and are therefore not fully understood.

1.3. *Objective of present work*

The underlying flow physics associated with LSBs is very challenging as both separation and transition occur simultaneously and are intricately linked. The situation becomes even more complex in the presence of FST, where the different instability mechanisms can compete with one another. The main objective of the present numerical investigations is to gain an improved understanding of the relevant physical

mechanisms governing LSBs in general and the transition process in particular, in the presence of FST. As mentioned in the previous section, increasing the FST levels causes stronger K-modes and thus leads to accelerated transition. However, increasing the FST level alone could not explain how the K-modes become the dominant instability mechanism when considering the fact that K-modes have a low (algebraic) growth rate compared to the high amplification rate associated with the KH instability. The present work is motivated by the need for additional insight into the Klebanoff instability mechanism in the presence of the separated shear layer. Therefore, in the present work, the streamwise evolution of unsteady K-modes from the initial linear stage, in the approach (attached) boundary layer, up to the nonlinear stage is investigated in detail. Towards this end extremely large computing times are required due the low-frequency characteristics of the K-modes.

Transitional LSBs, specially when subjected to FST, consist of flow structures with different dominant frequencies and wavelengths so that instantaneous flow visualizations do not provide a complete understanding regarding the underlying flow physics. Therefore, a detailed analysis of the simulation data using spectral analysis and modal decompositions is employed in order to provide additional insight into the underlying flow physics for various FST intensities. Furthermore, detailed investigations are carried out to investigate if and how the FST energy spectrum used in the FST model affects the transition process and the mean flow characteristics of LSBs. The rest of the paper is organized as follows: the next section, § 2, describes the computational set-up, governing equations, numerical methods and the FST generation procedure. A detailed discussion of the results is provided in § 3. A summary of the results and the contributions of the paper are given in § 4.

2. Direct numerical simulations

DNS of transition requires numerical methods for solving the Navier–Stokes equations that have low numerical dispersion and dissipation. Therefore, a 3D incompressible Navier–Stokes code using a combination of high-order-accurate finite-difference approximations and a pseudo-spectral method was employed for the DNS. This code was developed in our Computational Fluid Dynamics (CFD) Laboratory and validated for numerous cases of boundary-layer transition (Meitz & Fasel 2000), LSBs in 2D and 3D boundary layers (Hosseinverdi, Balzer & Fasel 2012; Balzer & Fasel 2016; Hosseinverdi & Fasel 2016) and separation control (Postl, Balzer & Fasel 2011; Hosseinverdi & Fasel 2013*b*, 2018). The following section provides a description of the simulation set-up, the governing equations and the computational approach used for solving the 3D, unsteady, incompressible Navier–Stokes equations.

2.1. *Simulation set-up*

The simulations set-up was guided by water-tunnel experiments that were carried out in the Hydrodynamics Laboratory at the University of Arizona (Radi & Fasel 2010; Chetan & Fasel 2012). In the experiments, the LSBs are generated on a flat plate through the close proximity of an inverted wing with a modified NACA 643-618 airfoil (see figure 1). Suction is applied in the aft part of the airfoil to prevent flow separation from the airfoil such that flow separation and reattachment occur only on the flat plate.

For our simulations, we employ our high-order-accurate, spatial DNS code for a model geometry (separation is generated on a flat plate as in the experiments). This model geometry is defined such that it exhibits a flow with similar physical

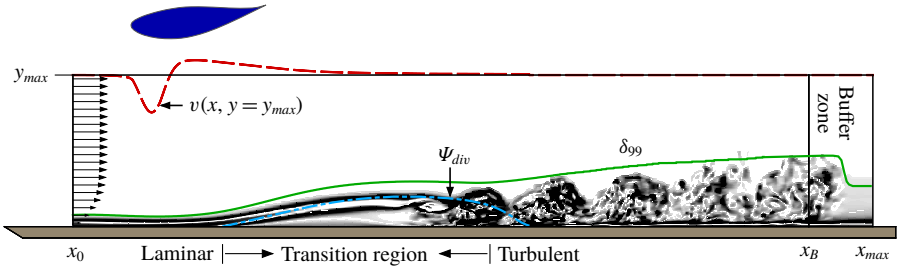

FIGURE 1. (Colour online) Schematic side view of the computational set-up (drawing not to scale). The domain extent in the streamwise direction is $x_0 = 1 \leqslant x \leqslant x_{max} = 17.19$, and the domain height is $y_{max} = 2$. The buffer region starts at $x_B = 16$. Indicated are the typical wall-normal velocity distribution applied at the upper boundary (dashed red line), the velocity profile at the inflow and the buffer zone near the outflow. Also shown are instantaneous contours of spanwise-averaged ω_z vorticity, the mean boundary-layer thickness (solid green line) and the dividing streamline (blue dot-dash curve).

properties as the flow over an airfoil but at reduced geometric complexity. This approach will enable higher grid resolution and the use of a considerably more efficient incompressible DNS code that will allow us to capture the relevant physics with greater confidence.

The governing equations are solved inside a rectangular integration domain as shown schematically in figure 1. The integration domain does not include the leading edge. The streamwise coordinate is x, the spanwise coordinate is z and the wall-normal coordinate is y. Length scales were made dimensionless using a reference length $L^*_\infty = 0.1$ m and velocities were made dimensionless with a free-stream velocity $U^*_\infty = 0.028$ m s^{-1}. The Reynolds number based on displacement thickness and the local free-stream velocity at the inflow boundary and the separation point are $Re_{\delta_1} = 160$ and $Re_{\delta_1} = 297$, respectively. The Reynolds number based on the separation length (l), the distance between mean reattachment and separation location, varies from $Re_l \approx 1.05 \times 10^4$ to $Re_l \approx 1.91 \times 10^4$ depending on the intensity of incoming FST fluctuations.

The domain width in the spanwise direction is $L_z = 3$. The spanwise domain width was selected based on the maximum bubble height (von Terzi 2004; Jones *et al.* 2008). A domain width of at least four times the maximum bubble height is necessary to resolve the largest spanwise structures. The ratio of domain width and the maximum bubble height ranges from 7.6 to 12.5 for the lowest and the highest FST intensities investigated here. Furthermore, the effect of the spanwise extent of the computational domain was investigated in detail in our previous research (Hosseinverdi *et al.* 2012) for the same simulation set-up. It was demonstrated that the current domain width ($L_z = 3$) is large enough not to affect the main characteristics of the separation bubble, such as the bubble length and the skin-friction distribution.

2.2. *Governing equations*

The governing equations are the incompressible, unsteady Navier–Stokes equations in vorticity–velocity formulation. The transport equation for the vorticity vector $\boldsymbol{\omega}$ is

$$\frac{\partial \boldsymbol{\omega}}{\partial t} = \boldsymbol{\nabla} \times (\boldsymbol{u} \times \boldsymbol{\omega}) + \frac{1}{Re} \nabla^2 \boldsymbol{\omega}. \tag{2.1}$$

Here the vorticity is defined as the negative curl of the velocity $\boldsymbol{\omega} = -\boldsymbol{\nabla} \times \boldsymbol{u}$. Equation (2.1) consists of three transport equations for the vorticity components in the streamwise (x), wall-normal (y) and spanwise (z) directions, respectively. In the above equation, the global Reynolds number is defined as $Re = U^*_\infty L^*_\infty / \nu^*$, where ν^* is the kinematic viscosity. The asterisk is used to denote dimensional quantities.

Using the fact that both the vorticity and velocity vector fields are solenoidal, one can obtain a vector Poisson equation for the velocity field,

$$\nabla^2 \boldsymbol{u} = \boldsymbol{\nabla} \times \boldsymbol{\omega}. \tag{2.2}$$

2.3. *Numerical methods*

The governing equations are integrated in time using an explicit fourth-order-accurate Runge–Kutta scheme. All derivatives in streamwise and wall-normal directions are approximated with fourth-order compact differences. No explicit filtering is used in the present investigations. Instead, stability is enhanced by appropriate treatment of the first derivative of the nonlinear terms, which are discretized using fourth-order-accurate (split) compact differences in the x-direction. At consecutive substeps of the four-stage Runge–Kutta scheme, the numerical scheme alternates between upwind-biased differences and downwind-biased differences. In the wall-normal direction, an exponential grid stretching is used in order to cluster grid points near the wall. Note that the finite-difference approximations for the derivatives with respect to y are constructed for a non-equidistant grid instead of using a coordinate transformation. While this approach is tedious, it can yield higher accuracy than the traditional method of grid stretching by using a coordinate transformation.

The flow field is assumed to be periodic in the spanwise direction. Therefore, the flow field is expanded in Fourier cosine and sine series. Each variable is represented by a total of $2K + 1$ Fourier modes: the 2D spanwise average (zeroth Fourier mode), K symmetric Fourier cosine as well as K antisymmetric Fourier sine modes. To avoid aliasing errors, the nonlinear terms in physical space are computed on $\mathcal{K} \approx 3K$ spanwise collocation points. Fast Fourier transforms (FFTs) are employed to convert each variable from spectral space to physical space and vice versa. The nonlinear terms are computed in physical space, while differentiation, integration and imposition of boundary conditions take place in spectral space. For the calculation of the nonlinear terms, the flow field is transformed from spectral to physical space (and back) before each Runge–Kutta substep, which requires redistributing of the entire 3D arrays among the processors. This extensive inter-processor communication is realized using the message passing interface (MPI).

The velocity Poisson equation (2.2) is solved by a direct method using fourth-order standard compact differences in the wall-normal direction and Fourier sine transforms in the streamwise direction.

2.4. *Boundary conditions*

The flow enters the computational domain at the inflow boundary location, x_0, and leaves it through the outflow boundary at x_{max}. In the spanwise direction, the flow is assumed to be periodic with the fundamental wavelength $\lambda_z = L_z$, where L_z is the domain width in the spanwise direction.

At the inflow boundary at $x = x_0$, all velocity and vorticity components are specified. In particular, the velocity and vorticity components of a 2D steady-state basic flow obtained from the Falkner–Skan equations, which closely matches that of the

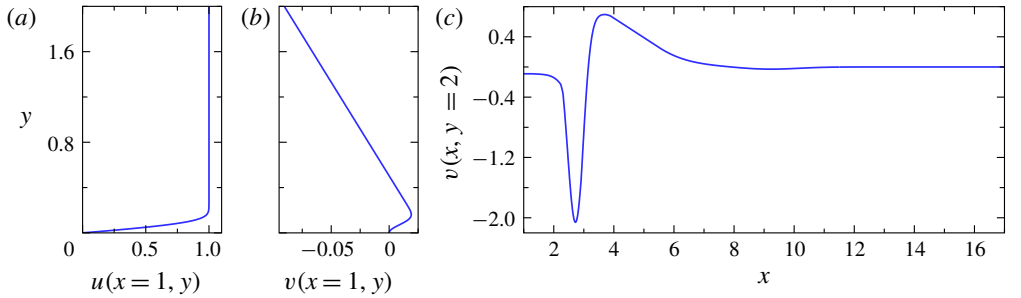

FIGURE 2. (Colour online) (*a*) Streamwise and (*b*) wall-normal velocity profiles at the inflow boundary of the computational domain; (*c*) v-velocity versus x imposed at the free-stream boundary (y_{max}).

experiments (see figure 2*a*,*b*), superimposed with velocity and vorticity fluctuations from the FST model, are prescribed as Dirichlet boundary conditions. In addition, for maintaining the fourth-order accuracy of the code near the inflow boundary, the streamwise derivatives of all dependent variables are prescribed as well.

At the outflow boundary, $x = x_{max}$, all second derivatives in the streamwise direction are set to zero. In addition, a buffer domain in the region $x_B \leqslant x \leqslant x_{max}$, as proposed by Meitz & Fasel (2000), is employed in order to smoothly dampen out the fluctuations generated inside the domain. Note that near the outflow boundary, the boundary layer is turbulent and large errors would occur if a laminar boundary-layer solution were enforced at the outflow boundary. Therefore, within the buffer region, the solution was ramped down to turbulent mean flow profiles, which were obtained from precursor simulations with a longer integration domain.

The no-slip and no-penetration conditions are enforced on the surface of the flat plate. In addition, the wall-normal derivative of the v-velocity is set to zero to ensure conservation of mass. At the free-stream boundary $y = y_{max}$, the wall-normal derivatives of all vorticity components are set to zero, thus allowing the vorticity to relax to some constant values (not necessarily zero). A wall-normal velocity distribution is applied at the upper boundary as a Dirichlet boundary condition for generating the favourable APGs that induce laminar separation on the flat plate. The v-velocity distribution is chosen such that the resulting downstream pressure gradient closely matches that of accompanying water-tunnel experiments as shown in figure 2(*c*). This method was also used by Alam & Sandham (2000) and Spalart & Strelets (2000). Such an approach can be viewed as the numerical equivalent to a displacement body or suction port in an experiment.

2.5. *Generation of free-stream turbulence in direct numerical simulations*

The LSBs investigated here are subjected to the FST, which was modelled by introducing a set of velocity and vorticity disturbances at the inflow boundary of the domain. The methodology adopted for generating realistic FST velocity fluctuations at the inflow boundary is similar to that proposed by Jacobs & Durbin (2001) and Brandt *et al.* (2004). The method is based on a Fourier expansion of the disturbance velocity with random amplitudes:

$$\boldsymbol{u}'(\boldsymbol{x}, t) = \sum_k \hat{\boldsymbol{u}}(\boldsymbol{k}, t) \mathrm{e}^{\mathrm{i}\boldsymbol{k}\cdot\boldsymbol{x}}, \tag{2.3}$$

where the wavenumber vector is $\boldsymbol{k} = [k_x, k_y, k_z]^{\mathrm{T}}$ with $k = |\boldsymbol{k}|$. Here k_x, k_y and k_z are the streamwise, wall-normal and spanwise wavenumbers, respectively. In the same manner, the inflow disturbance vorticity field is calculated from the disturbance velocity field as $\boldsymbol{\omega}' = -\boldsymbol{\nabla} \times \boldsymbol{u}'$.

The objective is to specify the Fourier coefficients of a disturbance velocity field such that the inlet disturbance flow field satisfies continuity and generates isotropic turbulence in the free stream and models a specified energy spectrum. By invoking Taylor's hypothesis and ignoring the streamwise decay, $k_x x$ can be replaced by $-\omega t$, where ω is the angular disturbance frequency. The implementation of the spanwise Fourier modes, $\mathrm{e}^{\mathrm{i}k_z z}$, is straightforward since the numerical model assumes periodicity of the flow field in the z-direction. However, in the presence of an inhomogeneous y-direction, specific basis functions are needed to account for the presence of the wall. Instead of Fourier modes $\mathrm{e}^{\mathrm{i}k_y y}$ in the expansion of the disturbance quantities, Jacobs & Durbin (2001) and Brandt *et al.* (2004) suggested to use eigenmodes from the continuous spectrum of the Orr–Sommerfeld and Squire operators since they are sinusoidal in the free stream, but naturally decay inside the boundary layer (see Grosch & Salwen 1978). Therefore (2.3) can be reformulated as

$$\boldsymbol{u}'(x_0, y, z, t) = \sum_{\omega} \sum_{k_z} \sum_{k_y} A(k) \boldsymbol{\Phi}(y; \omega, k_y, k_z) \mathrm{e}^{-\mathrm{i}\omega t} \mathrm{e}^{\mathrm{i}k_z z}. \tag{2.4}$$

Here, the coefficients $A(k)$ determine the contribution of the eigenfunctions to the total turbulent kinetic energy and $\boldsymbol{\Phi}$ is a normalized weighted superposition of Orr–Sommerfeld and Squire continuous eigenfunctions. The velocity fluctuations at the inflow model the specified energy spectrum. Various analytic forms for the energy spectrum exist. For most of the simulations presented in this work, the von Kármán energy spectrum is employed for distributing the turbulent kinetic energy among the various modes,

$$E(k) = Tu_0^2 L_{11} \frac{1.196(kL_{11})^4}{0.558[1 + (kL_{11})^2]^{17/6}}. \tag{2.5}$$

The turbulent integral length scale, L_{11}, determines the wavenumber associated with the maximum in the $E(k)$ distribution. For large scales (small k) the spectrum is asymptotically proportional to k^4. For small scales (large k) the spectrum matches Kolmogorov's $k^{-5/3}$ law.

In order to obtain isotropic turbulence, several wavenumbers k have to be selected in the domain $k_{min} \leqslant k \leqslant k_{max}$, where the limiting wavenumbers are determined by the chosen numerical resolution. For the present simulations, $k_{min} = 2$ and $k_{max} = 100$ were used. The smallest and largest spanwise wavenumbers that are resolved by the DNS are $k_{z,min} = 2.09$ and $k_{z,max} = 131.95$. For the present investigations, the wavenumber space (k) was divided into 40 equidistant concentric shells over which energy was distributed discretely using a limited number, N_p, of disturbance modes. Modes on a given shell have an identical wavenumber magnitude, $k = (\omega^2 + k_y^2 + k_z^2)^{0.5}$. The coefficient of each term in (2.4) is given by $A(k) = \sqrt{2E(k)\Delta k / N_p}$, where Δk is the difference in wavenumber between two shells. Finally, upon choosing the parameters L_{11} and the FST intensity Tu_0, the inflow velocity and vorticity disturbance fields can be entirely determined. Detailed descriptions of the implementation and validation results are provided in Hosseinverdi *et al.* (2012), Balzer & Fasel (2016) and Hosseinverdi & Fasel (2018). It is worth noting that FST fluctuations are introduced at the inflow boundary of the computational domain, which is downstream of the leading edge. Thus, the effect of the leading edge on the receptivity process with respect to free-stream disturbances as encountered in experiments is neglected in this approach.

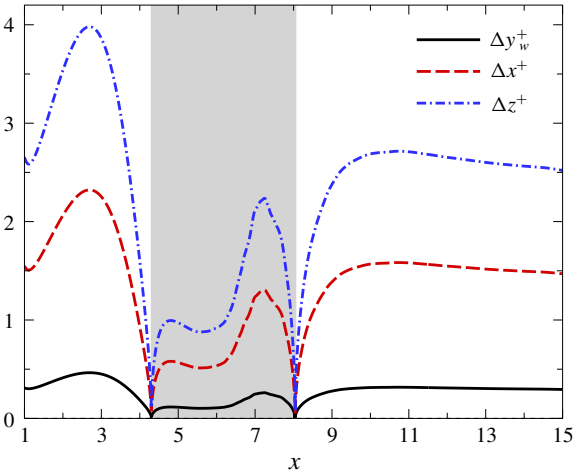

FIGURE 3. (Colour online) Grid spacing in wall coordinates. Data from case with $Tu_0 = 3\,\%$. The shaded area corresponds to the mean separation length.

2.6. *Assessment of grid resolution*

All the simulations presented in this work are carried out using the same computational grid with a resolution of $N_x \times N_y \times N_z = 1851 \times 240 \times 200 \approx 89$ million grid points. The grid spacing is uniform in the streamwise direction and the grid points are exponentially displaced from the wall in the wall-normal direction with an expansion ratio below 1.015 to improve the resolution near the wall. In the spanwise direction, 127 Fourier modes (200 collocation points) were employed.

A useful analysis of grid resolution is to transform the grid spacing to wall units. The wall units for the streamwise, spanwise and wall-normal (adjacent to the wall) directions for the case with an inflow FST intensity of 3 % is provided in figure 3. The grid resolution within the separation bubble and in the redeveloping turbulent boundary layer downstream of the reattachment point is $\Delta x^+ \leqslant 1.58$, $\Delta z^+ \leqslant 2.71$ and $\Delta y_w^+ \leqslant 0.32$. The grid resolutions in wall units are calculated according to $(\Delta)^+ = (\Delta) Re (c_f/2)^{0.5}$.

A comparison of the grid resolution used by other authors is given in table 1. These values are based on a skin-friction value of $c_f \approx 8.36 \times 10^{-3}$. This value corresponds to the maximum skin-friction coefficient in the redeveloping turbulent boundary layer. The grid resolution in the presented simulations is finer compared to the resolutions used in the available literature. To justify that this grid resolution is sufficient to resolve all the relevant length scales in the interior of the flow, the grid line spacing is compared to an estimate of the Kolmogorov length scale η, characterizing the length scale of the dissipative motion (Pope 2001). The length scale is obtained from the dissipation rate given by

$$\eta = (Re^3 \varepsilon)^{-1/4}, \tag{2.6}$$

where ε is the turbulent dissipation rate determined from

$$\varepsilon = \frac{1}{Re} \overline{\left(\frac{\partial u_i'}{\partial x_j}\right)\left(\frac{\partial u_i'}{\partial x_j} + \frac{\partial u_j'}{\partial x_i}\right)}. \tag{2.7}$$

The overbar denotes the time average and the prime indicates fluctuation quantities with respect to the mean. The ratio of the grid line spacing in the wall-normal

Case	Δx^+	Δy^+ at $y^+ = 9$	Δz^+	$N(y^+ < 9)$
Alam & Sandham (2000), case 3DF-B	14.26	0.87	6.3	17
Jones *et al.* (2008), case 3DF	3.36	$\geqslant 1$	6.49	$\leqslant 9$
Marxen & Henningson (2011), case reso1	6.53	0.94	11.06	10
Balzer & Fasel (2016)	5.6	0.9	6.15	18
Present simulations with $Tu_0 = 3\,\%$	1.58	0.44	2.71	25

TABLE 1. Comparison of grid resolution in wall units with other simulations.

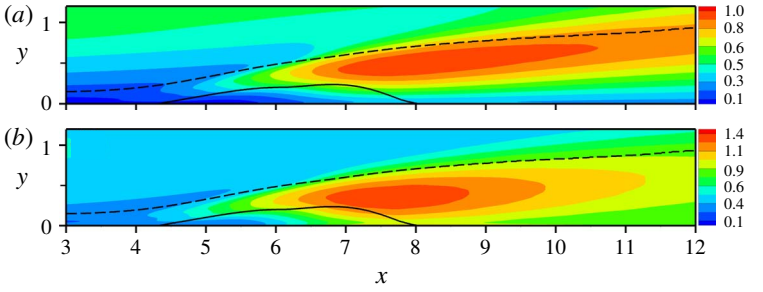

FIGURE 4. (Colour online) Contours of ratio of grid spacing to the Kolmogorov length scales for $Tu_0 = 3\,\%$: (*a*) $\Delta y/\eta$, (*b*) $\sqrt[3]{\Delta x \times \Delta y \times \Delta z}/\eta$. Dashed lines are the time- and spanwise-averaged boundary-layer thickness and solid line is the mean dividing streamline.

direction to the Kolmogorov length scale, $\Delta y/\eta$, is plotted in figure 4(*a*). As can be seen, the grid line spacing in the wall-normal direction is smaller than η in the entire domain. The ratio of Δ/η, where $\Delta = \sqrt[3]{\Delta x \times \Delta y \times \Delta z}$, is presented in figure 4(*b*). The ratio increases to 1.3 in the aft portion of the separation bubble. This is due to the fact that Δx and Δz are slightly larger than Δy. Typically, the smallest length scale that needs to be resolved is of $O(\eta)$ and not exactly equal to η; Moser & Moin (1987), for example, showed that most of the dissipation in the curved channel occurs at scales greater than 15η. Consequently, these observations warrant that the present simulations are exceptionally well resolved.

3. Results

In this section, results obtained from DNS of LSBs for various levels of FST intensity are discussed in detail. For the present investigations, FST intensities were $Tu_0 = 0$, 0.1 %, 0.5 %, 1 %, 2 % and 3 %, where Tu_0 is the FST intensity at the inflow boundary defined as $Tu_0 = (\frac{1}{3}[\overline{u'u'} + \overline{v'v'} + \overline{w'w'}])^{0.5}$, where the overbar denotes the time average. Here, $Tu_0 = 0$ corresponds to the zero FST simulation where no external disturbances were introduced into the flow. A detailed analysis of the simulation data based on the instantaneous flow structures, spectral analysis and modal depositions is carried out to explore if and how the FST affects the fundamental flow physics compared to the LSB without FST.

3.1. *Instantaneous flow structures*

Owing to the large growth rates associated with the separated shear layer, the disturbances can be amplified by several orders of magnitude, which leads to

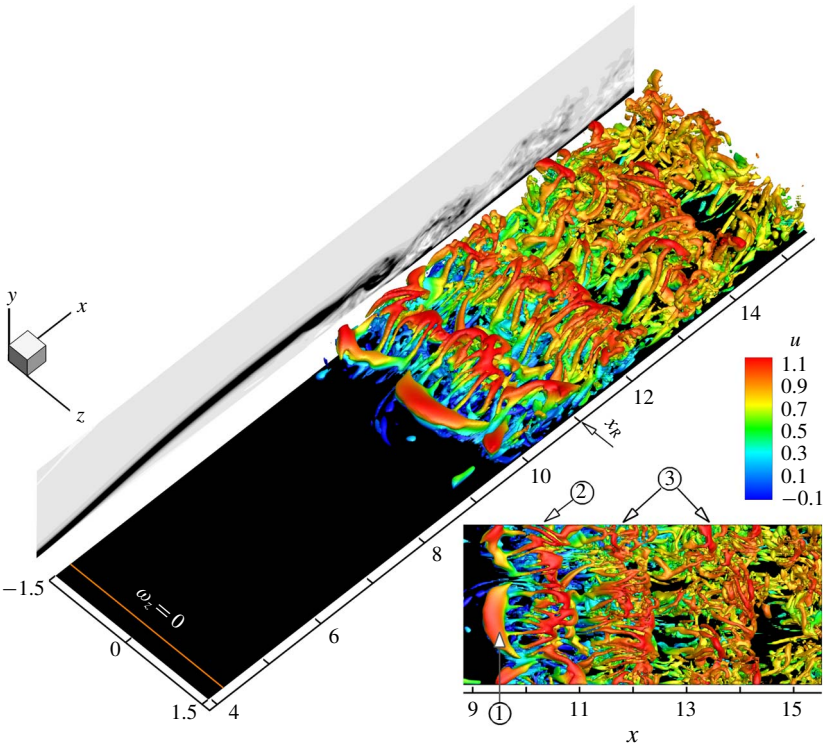

FIGURE 5. (Colour online) Instantaneous flow visualizations for the case without FST. Plotted are isosurfaces of $\lambda_2 = -0.75$ coloured by u-velocity in perspective and top-down views. The separation line is indicated by $\omega_z = 0$ at the wall and x_R shows the mean reattachment location. Plotted in the x–y plane are the contours of spanwise vorticity (averaged in spanwise direction).

the development of large unsteady vortical structures that can persist even in the turbulent flow region downstream of the reattachment location (coherent structures). Furthermore, FST can induce additional disturbance waves inside the boundary layer, which contribute to the laminar–turbulent transition process.

To gain insight into the nature of the vortical structures and their evolution, the instantaneous isosurfaces are visualized in figure 5 using the λ_2-criterion by Jeong & Hussain (1995) coloured by u-velocity together with the contours of spanwise vorticity (averaged in spanwise direction) for a zero FST. The separation line, $\omega_z = 0$, is also indicated at the wall by the solid line. Starting from the left in figure 5, the boundary layer separates at $x_s = 4.26$, followed by a very smooth separated shear layer, which has no noticeable dependence in the spanwise direction. The thickness of the separated shear layer increases downstream of the separation location. Through the contours of spanwise vorticity, it is found that the separated shear layer rolls up and grows in intensity due to the KH instability as it is convected downstream. This is followed by shedding of strong coherent (clockwise-rotating) vortices (often referred to as 'rollers'), and finally leading to turbulent reattachment. It should be noted that in our previous research (see Hosseinverdi & Fasel 2013*a*) for the same simulation set-up, we found that transition to turbulence appeared to be self-sustained for zero FST, i.e. in contrast to zero-pressure-gradient boundary layers, no external forcing was required to initiate

or sustain the transition process. It was demonstrated that the development of 3D disturbances is due to an absolute secondary instability.

The λ_2-criterion indicates large spanwise-oriented structures near $x = 9.4$, labelled 1 in figure 5. It corresponds to the spanwise rollers or KH vortices. Previous research (Marxen *et al.* 2003; Rist 2003; Postl *et al.* 2011; Hosseinverdi *et al.* 2012) suggests that these structures result from the large-amplitude 2D disturbances associated with the primary (KH) instability of the streamwise mean flow profile. Large-scale vortices facilitate the transfer of high-momentum fluid from the free stream towards the wall and of low-momentum fluid away from the wall, and, as a consequence, accelerate reattachment. In figure 5, the structure labelled 2 is a spanwise dominant vortex that has recently been shed from the separated shear layer. Further downstream, the flow breaks down into smaller structures. It can be seen that the small scales are still organized in a spanwise coherent structure, labelled 3. These coherent structures persist even downstream of reattachment.

The picture changes when isotropic FST is introduced at the inflow boundary. Hydrodynamic instability of laminar separated shear layers makes the LSB highly susceptive to FST. Therefore, the onset of transition is moved upstream compared to the zero FST when the FST level is increased to $Tu_0 = 0.5\,\%$ (see figure 6), which in turn leads to a reduction of the separated flow region. Instantaneous isosurfaces of the λ_2-criterion are presented in figure 6 together with the contours of streamwise and spanwise vorticity at several selected planes. One KH roller is visible before the flow breaks down to smaller scales. For this case, the reattaching flow is organized by the vortices coherent in the spanwise direction. Predominantly spanwise structures are indicative of the dominant 2D waves in the transition region and highlight their role as a viable path to turbulence.

Judging from figures 5 and 6, KH vortices are more 2D for case with $Tu_0 = 0.5\,\%$ than for zero FST simulation. As mentioned earlier, transition to turbulence is due to an absolute secondary instability for the natural LSB (zero FST), implying that the disturbances (due to numerical and round-off errors) propagate in both the downstream and upstream directions while being amplified in time and ultimately result in vortex shedding leading to transition. A similar observation was reported in Jones *et al.* (2008), where 'rollers' are not purely 2D for uncontrolled LSB. The onset of unsteadiness was also due to an absolute secondary instability in their work. In contrast to the disturbance-free simulation (zero FST), the amplitude level of the incoming 2D disturbance waves is elevated in the presence of FST (orders of magnitude higher than in the zero FST case). Considering that 2D modes are the most amplified instability waves in low-disturbance environments (Marxen *et al.* 2003, 2004), the primary convective instability strongly (by orders of magnitudes) amplifies the disturbance waves within the KH frequency range of the separated shear layer leading to the organized spanwise structures for $Tu_0 = 0.5\,\%$.

From experiments and numerical simulations (Klebanoff & Tidstrom 1959; Klebanoff 1971; Jacobs & Durbin 2001; Fasel 2002; Goldstein 2014), it is known that the FST can cause the formation of streamwise-elongated streaks inside the boundary layer that are caused by the so-called Klebanoff modes (K-modes). For this case, the Klebanoff modes have very small amplitudes and can be visualized by looking at the streamwise vorticity component as shown in the top-left plot in figure 6 at two different x locations and on the wall. The contours of streamwise vorticity at $x = 3$ show that the vortical disturbances are present in the free stream. The free-stream vortical disturbances permeate into the boundary layer and manifest themselves as the counter-rotating longitudinal vortices as illustrated by the streamwise vorticity at

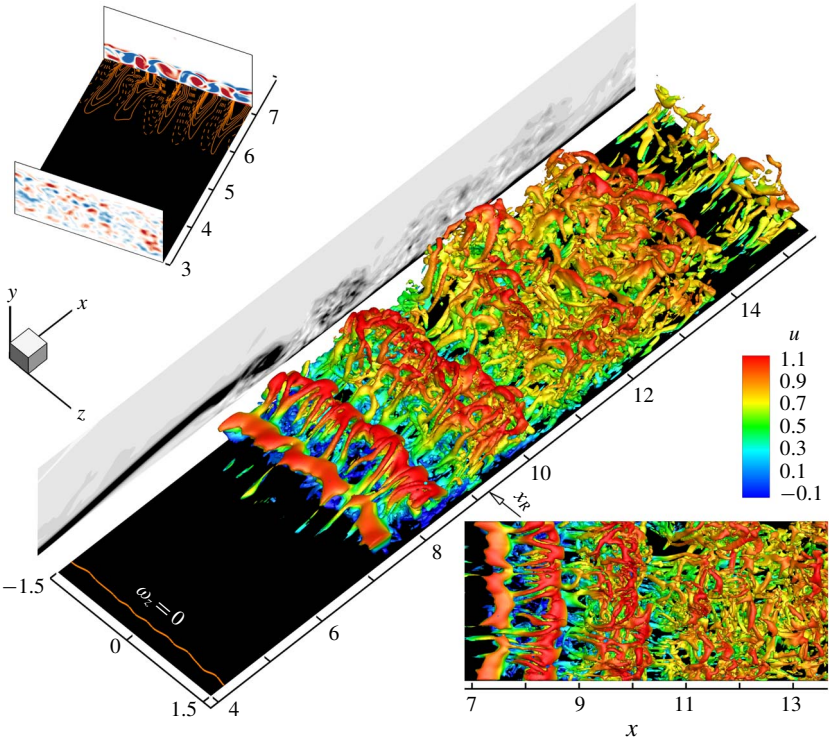

FIGURE 6. (Colour online) Isosurfaces of $\lambda_2 = -0.75$ coloured by u-velocity in perspective and top-down views for the case with $Tu_0 = 0.5\,\%$. Plotted in the x–y plane are the contours of spanwise vorticity (averaged in the spanwise direction). Top-left: contours of streamwise vorticity at $x = 3$ and 7 and wall streamwise vorticity (dashed contour lines indicate $\omega_x < 0$). Contour line of $\omega_z = 0$ corresponds to the instantaneous separation line and x_R shows the mean reattachment location.

the wall with a preferred spanwise wavelength of $\lambda_{z,K} \approx L_z/5$, which can be clearly observed for example at slice $x = 7$. These counter-rotating vortices facilitate the exchange of momentum by transporting the low-momentum fluid away from the wall and pushing the high-momentum fluid towards the wall. Furthermore, the spanwise spacing of Klebanoff modes based on the local boundary-layer thickness, δ, is of the order of $\lambda_{z,K} \approx O(2.65\delta$–$4\delta)$ for $3 \leqslant x \leqslant x_s$, which is consistent with the findings of $\lambda_{z,K} \approx O(2\delta$–$4\delta)$ for attached flat-plate boundary layers (Kendall 1985, 1990; Westin *et al.* 1994). Contrary to the case with zero FST, the boundary-layer fluctuations associated with the K-mode have a local effect on the instantaneous separation line as it is now modulated in the spanwise direction.

From instantaneous flow visualization for the highest FST intensity investigated ($Tu_0 = 3\,\%$) shown in figure 7, it appears that the separated shear layer loses its predominantly 2D character and exhibits oblique spanwise-oriented structures that deteriorate due to the large-amplitude streamwise streaks. This gives room to speculate that high FST intensities enhance the level of 3D disturbances and that these eventually dominate the 2D waves. The traces of K-modes could also be identified in the λ_2 structures as the K-modes become stronger for elevated FST levels.

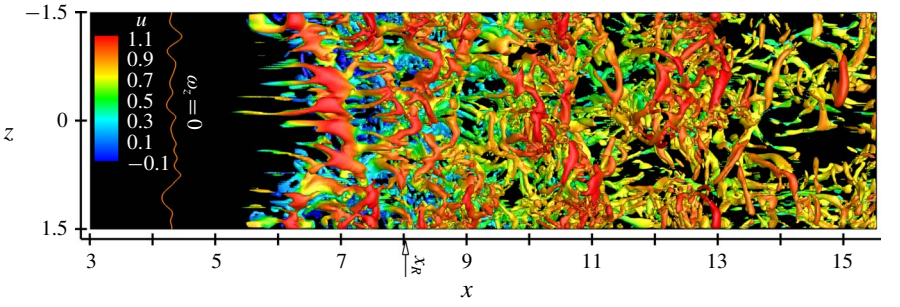

FIGURE 7. (Colour online) Isosurfaces of $\lambda_2 = -0.75$ coloured by u-velocity in top-down view for the case with $Tu_0 = 3\,\%$. The mean reattachment location is depicted by the arrow. The instantaneous separation line is indicated by $\omega_z = 0$ at the wall.

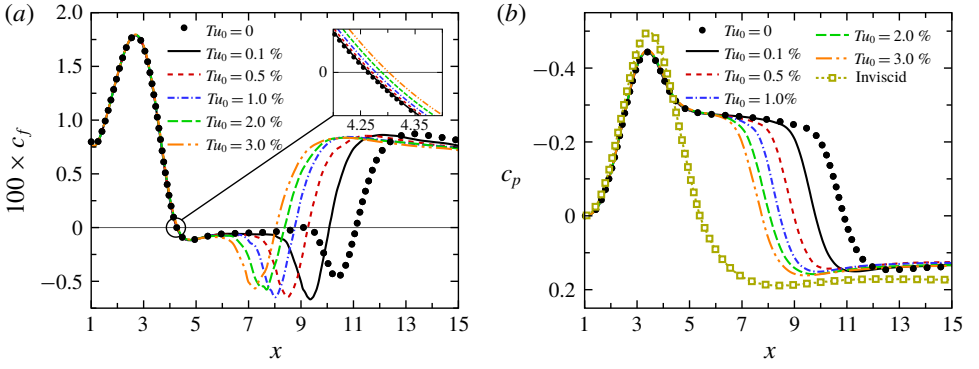

FIGURE 8. (Colour online) Time- and spanwise-averaged (*a*) wall-skin friction and (*b*) pressure coefficients for various levels of FST intensity.

3.2. *Time- and spanwise-averaged flow field*

In this section, the mean flow results for different FST intensities are compared and discussed. Towards this end, the DNS data were averaged in the spanwise direction as well as in time. Boundary-layer quantities from DNS, such as displacement thickness and momentum thickness, are computed based on a 'pseudo'-free-stream velocity. The pseudo-free-stream velocity was obtained from a wall-normal integral of the spanwise vorticity, ω_z, as suggested by Spalart & Strelets (2000).

Distributions of time- and spanwise-averaged wall skin-friction coefficients, c_f, and wall-pressure coefficients, c_p, are plotted in figure 8 for DNS with various FST intensities. With increasing FST levels, the mean reattachment point, at which c_f changes from negative to positive, moves upstream. The separation location, where c_f changes from positive to negative, remains almost constant, although a general trend can be observed that separation is slightly delayed for increased FST levels (see inset in figure 8*a*). The wall-pressure coefficient versus x shows a boundary-layer acceleration up to $x = 3.3$, which is the location of the minimum pressure. There is a plateau downstream of $x = 5$, which is an indication of the 'dead-air' region in the separation bubble (corresponding to the low velocities within the bubble). Included in figure 8(*b*) is the inviscid c_p distribution. It is difficult to classify the LSB investigated here as either 'short' or 'long' according to the Gaster criterion

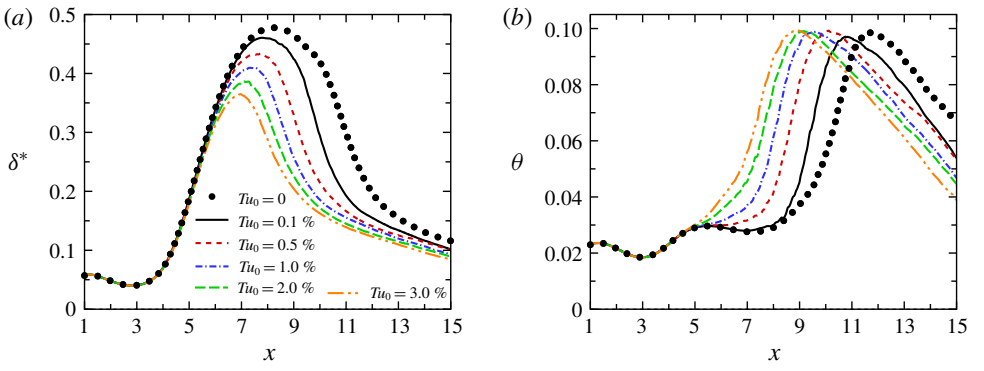

FIGURE 9. (Colour online) Comparison of boundary-layer parameters (time- and spanwise-averaged) for different FST intensities: (*a*) displacement thickness; and (*b*) momentum thickness.

(Gaster 1969), since the momentum thickness Reynolds number at the separation location, $Re_{\theta,s} \approx 83$, is below the minimum $Re_{\theta,s}$ used in his investigations. However, from figure 8(*b*), it is clear that the LSB alters the inviscid pressure distribution significantly. It can therefore be concluded that the LSBs, for all levels of FST examined, can be classified as 'long'.

The development of the boundary layer for different flow scenarios is compared in figure 9 by plotting the streamwise variation of the displacement thickness, δ^*, and the momentum thickness, θ. Downstream of $x = 4$, the rapid growth of the displacement thickness corresponds to the onset of the boundary-layer separation. From the displacement thickness distribution, it is found that, in addition to the reduction in separation bubble length, the height of the separation bubble also decreases with increasing FST intensity. While for the zero and low FST levels, the momentum thickness varies only slowly downstream of separation and across the stagnant flow region of the bubble, for the cases with higher FST levels, there is a rise in θ right downstream of the separation location. This change in the momentum thickness could be attributed to the spanwise redistribution of momentum within the boundary layer due to the FST. Another observation is the rapid rise in θ corresponding to the 'reverse-flow vortex' region which represents the process of shear-layer roll-up and shedding of vortices (in a time-averaged sense).

The time- and spanwise-averages of the streamwise velocity, u, at $y = 1$ and selected streamwise locations are compared with the experimental measurements in figure 10. For the comparison, the velocity profiles for cases without FST and FST intensities of 0.1 % and 0.5 % are considered here. It should be noted that the reported level of FST intensity in the experiment is $O(0.1\,\%–0.35\,\%)$. Despite the good agreement for the velocity profiles prior to the separation and the front part of the bubble ($x \leqslant 7.6$), the DNS data for the zero FST simulation indicate that reattachment occurred very far downstream compared to the experiments. Downstream of $x = 7.6$, the computed velocity profiles exhibit a larger distance of the separated shear layer from the wall. The discrepancy between the simulation and the experiments is likely due to an earlier onset of transition in the experiments, which could be attributed to the presence of FST disturbances in the experiments, imperfections of the surface and the like. These disturbances will of course accelerate transition, and, as a consequence, reduce the size of the separation bubble. Moreover, the circulation around the displacement

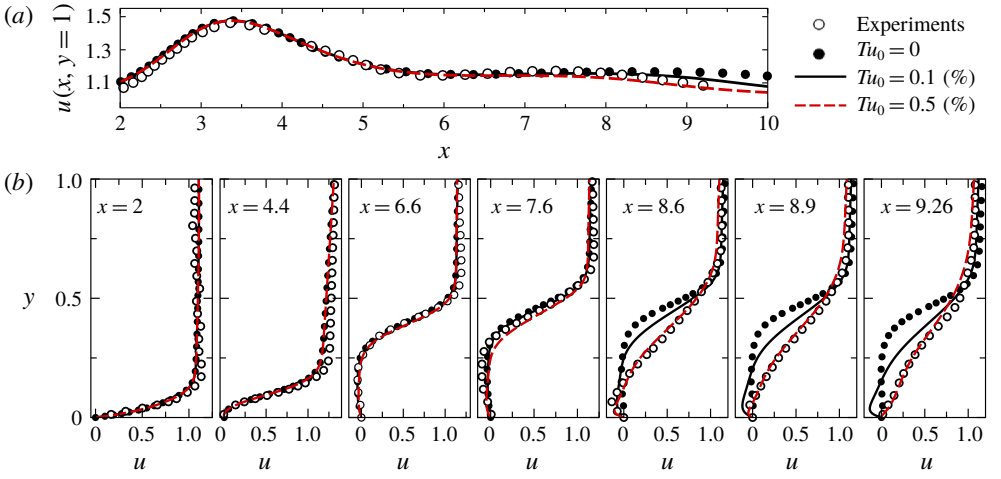

FIGURE 10. (Colour online) Time- and spanwise-averaged u-velocity compared to the experimental data (Radi & Fasel 2010; Chetan & Fasel 2012) at $y = 1$ (*a*) and several x locations (*b*).

body in the experiments, which could affect LSBs, is not present in the DNS. Such disturbances are not present in the DNS, except for a low level of background disturbances ('numerical noise'), which can be kept extremely small if, as in our case, high-order-accurate methods are used for solving the Navier–Stokes equations.

For the lowest FST level, $Tu_0 = 0.1\,\%$, the separation length and the thickness of the separation bubble are already reduced compared to the zero FST case; however, the best match is found for the case with $Tu_0 = 0.5\,\%$ for the profiles at the separation point, in the reverse-flow region and at the reattachment location. It is also worth noting that the discrepancy between the experimental and DNS results could partially be caused by differences in the spectral content of FST fluctuations used in DNS (2.5), as such an FST energy spectrum from the experiments was not available. To reproduce 'realistic' separation bubbles as observed in the experiments, it is therefore necessary to increase the background disturbance levels in the DNS to levels that are typical for experiments. As an alternative to introducing specified or random disturbances upstream of the separation, as done, for instance, by Marxen & Henningson (2011), we found it is more physical to introduce a realistic isotropic grid turbulence in the DNS.

The boundary layer downstream of the reattachment location is turbulent. However, it is very different from an equilibrium turbulent boundary layer as observed in the zero-pressure-gradient case. A more revealing look at the redeveloping turbulent boundary layer is provided in figure 11 for cases with $Tu_0 = 0.5\,\%$ and $Tu_0 = 3\,\%$. Plotted are the time- and spanwise-averaged flow quantities for several downstream locations using the near-wall scaling for turbulent boundary layers. Close to reattachment, the velocity profiles are very different from those of an equilibrium turbulent boundary layer. A slow relaxation of the velocity profiles towards the logarithmic law of the wall (given by the equation $u^+ = 2.44\,\log(y^+) + 0.5$) is observed. It is not until the furthest downstream location that the profiles approach equilibrium. A similar behaviour in the recovery region was reported by Na & Moin (1998) and Alam & Sandham (2000). The persistence of the dip below the log law can

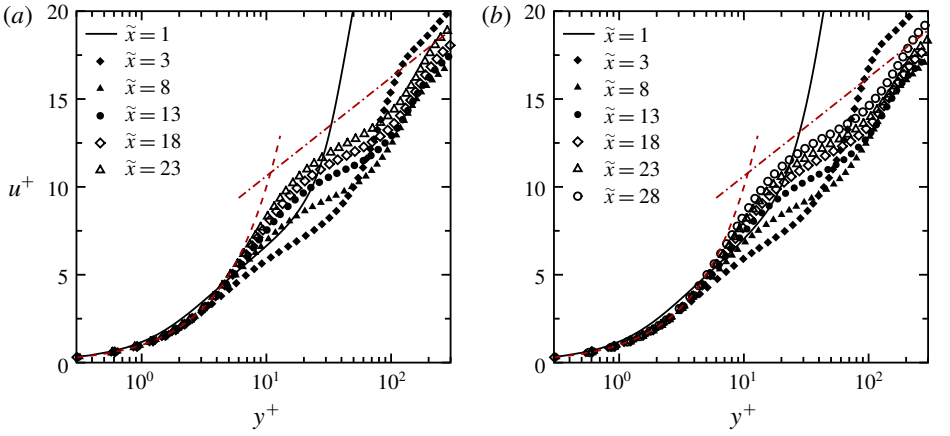

FIGURE 11. (Colour online) Streamwise velocity of the turbulent relaxing boundary layer in wall coordinates at various $\tilde{x}$ locations defined as $\tilde{x}=(x-x_R)/\delta_R^*$ where x_R and δ_R^* are the mean reattachment location and displacement thickness at x_R, respectively: (*a*) $Tu_0=0.5\,\%$; (*b*) $Tu_0=3\,\%$. Plots are time- and spanwise-averaged results. Dashed lines represent $u^+=y^+$ and dash-dotted line corresponds to $u^+=2.44\log(y^+)+0.5$.

be linked to the large coherent structures observed downstream of the reattachment location (see figure 6). These structures are embedded in the boundary layer and survive far downstream before breaking up into smaller dissipative eddies. In Alam & Sandham (2000) the turbulent boundary layer reached the log law of the wall at $\tilde{x}=24.43$, while in the present simulations for the case with $Tu_0=3\,\%$, at $\tilde{x}=28$, the velocity profile is still not in equilibrium. It should be noted that in the investigation of Alam & Sandham (2000) the relaxation process took approximately six bubble lengths while in the present simulations for the highest FST level, $Tu_0=3\,\%$ (shortest bubble length), the domain downstream of reattachment only extends two-and-a-half times the mean bubble length.

The results for mean flow presented in figures 8 and 9 indicated a reduction in separation length for increased levels of the incoming FST. However, the rate at which the separation region decreases as FST intensity increases is different for low and high FST intensities as shown in figure 12. It displays the mean separation length normalized by the momentum thickness at the separation location (θ_s) versus the turbulence intensity at the free stream at the separation location (Tu_s). For the cases with elevated FST, $1\,\% < Tu_0 \leqslant 3\,\%$, the mean separation length decreases at a lower rate compared to the cases with low to moderate FST intensities, $0.1\,\% \leqslant Tu_0 \leqslant 1\,\%$. Also, included in figure 12 is the variation of the maximum mean bubble height normalized with θ_s as a function of Tu_s, which shows a similar behaviour as the mean bubble length versus Tu_s.

From the instantaneous flow visualizations in figures 5–7, it appears that two mechanisms contribute to the exchange of momentum, which therefore play an important role in the reattachment process: (i) large-scale vortices that are being shed from the bubble as a result of the shear-layer roll-up and (ii) small vortical structures that are generated near the wall due to the breakdown of these large-scale structures. The shear-layer roll-up produces large mean tangential momentum ($\bar{u}\bar{v}$) while the breakdown of these large-scale vortical structures (spanwise 'rollers'), which contributes to the transition/reattachment processes, induces Reynolds shear

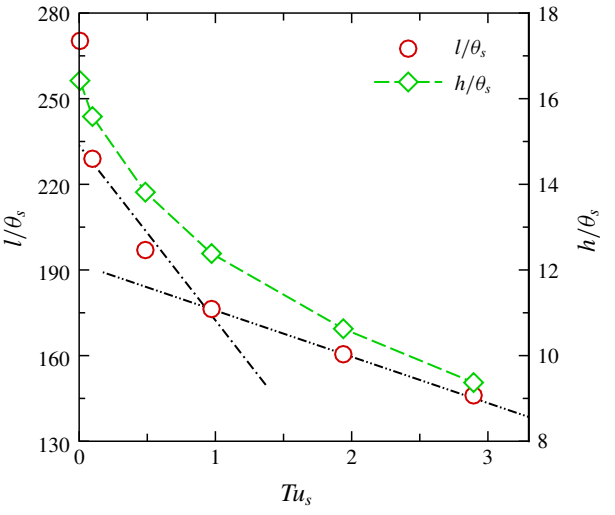

FIGURE 12. (Colour online) Variation of mean separation length, l, and the maximum bubble height, h, as a function of turbulence intensity in the free stream at the separation location, Tu_s. Both l and h are normalized by the momentum thickness at the separation location.

stress ($\overline{u'v'}$). According to Satta *et al.* (2007) and Simoni, Ubaldi & Zunino (2014), the negative values of the wall-normal derivatives of these components will accelerate the flow in the x-direction and therefore facilitate the reattachment process.

Figure 13 displays the contours of $-\partial(\bar{u}\bar{v})/\partial y$ and $-\partial(\overline{u'v'})/\partial y$ together with the time- and spanwise-averaged streamlines for different FST levels. It should be noted that contour levels are $0 \leqslant -\partial(\bar{u}\bar{v})/\partial y \leqslant 0.4$ and $0 \leqslant -\partial(\overline{u'v'})/\partial y \leqslant 0.15$ in figure 13. The wall-normal derivative of $\bar{u}\bar{v}$ acts mainly outside the separation bubble and reaches a maximum in the aft part of the bubble, the location where the separated shear layer sheds spanwise vortices (see figure 6). In contrast, an appreciable magnitude of the wall-normal derivative of the Reynolds shear stress is present inside the separated region and attains the maximum value further downstream, near the reattachment location, and is mainly confined close to the wall. Included in figure 13(*a*) are the loci of the (mean) inflection points. Of particular interest is the observation that the maxima of $-\partial(\bar{u}\bar{v})/\partial y$ occur very close to the mean inflection points, thus supporting the conjecture that the main contribution to this term is the inviscid shear-layer instability that produces the boundary-layer roll-up. Besides the spanwise 'rollers', it is important to point out that the term $-\partial(\bar{u}\bar{v})/\partial y$ contains (small) contributions from the fluctuations in the form of the Reynolds stresses as well. While the maximum of $-\partial(\overline{u'v'})/\partial y$ remains almost unchanged, the maximum of $-\partial(\bar{u}\bar{v})/\partial y$ is significantly reduced for cases with $Tu_0 > 1\,\%$. This reduction can be attributed to: (i) a stabilization of the convective instability of the separated boundary layer associated with the smaller mean LSB (due to the faster transition), and (ii) weakening of the spanwise-oriented structures by large-amplitude K-modes as was observed in figure 7, for example.

3.3. *Spectral analysis*

To analyse the unsteady fluid dynamics and understand the dominant laminar–turbulent transition mechanisms for different FST levels, the Fourier spectra of the time-

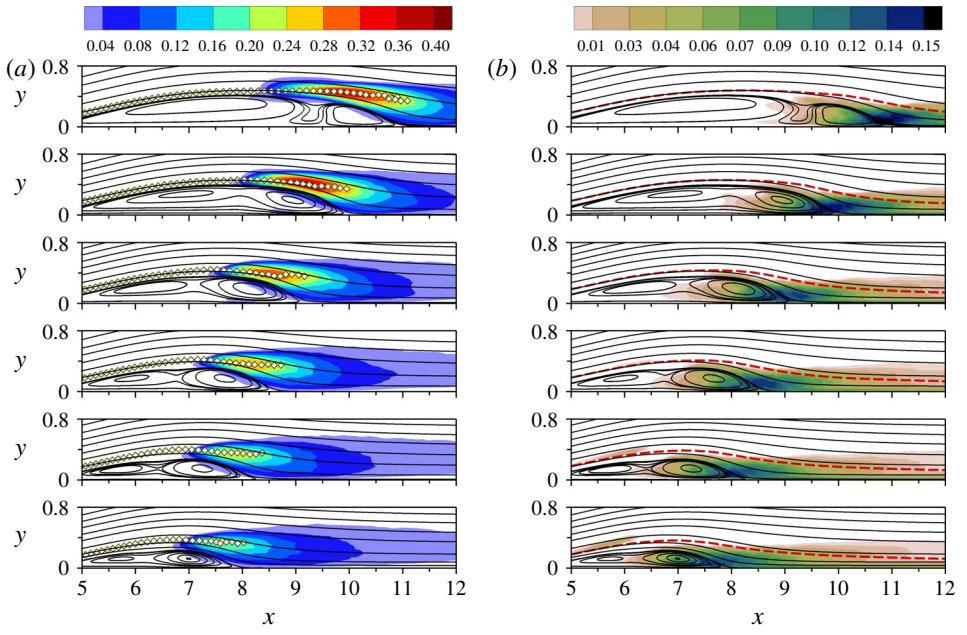

FIGURE 13. (Colour online) Contours of $-\partial(\bar{u}\bar{v})/\partial y$ (*a*) and $-\partial(\overline{u'v'})/\partial y$ (*b*) together with time- and spanwise-averaged streamlines. From top to bottom: $Tu_0 = 0$, 0.1 %, 0.5 %, 1 %, 2 % and 3 %. The symbols in (*a*) indicate the loci of mean inflection points and the dashed red lines in (*b*) correspond to the mean displacement thickness.

dependent velocity field in time and spanwise directions are evaluated. Note that the results obtained from the simulations are already in Fourier space in the z-direction. Hence, no transform in the spanwise direction has to be performed.

For zero FST simulation, typical time traces and the respective frequency spectra of the wall-normal disturbance velocity (averaged in spanwise direction) are presented in figure 14 for several streamwise locations within the bubble and downstream of the reattachment location. The data are extracted along the local displacement thickness, which is very close to the inflection point of the streamwise velocity component. Here, the dimensional frequency is non-dimensionalized as follows:

$$F = \frac{2\pi f^* \nu^*}{U_\infty^{*\,2}} \times 10^6. \tag{3.1}$$

Downstream of the separation point at $x = 8.5$, the time signals are reminiscent of 'modulated wave-trains' qualitatively similar to those observed by Schubauer & Skramstad (1948) in their 'natural' transition experiments of a flat plate boundary layer. The corresponding frequency spectra (figure 14*b*) exhibit a dominant frequency peak, which is caused by the growth of instability waves in the separated region. These instabilities lead to the 'periodic' shedding of the separation bubble with fundamental frequency of $F \approx 954$. Strong higher harmonics that are generated nonlinearly can be observed for $x \leqslant 10$.

Contours of the Fourier amplitude of the wall-normal disturbance velocity in the frequency F–x plane are shown in figure 15(*a*) for the case with FST intensity of 0.5 %. The Fourier amplitudes are averaged in the spanwise direction and the

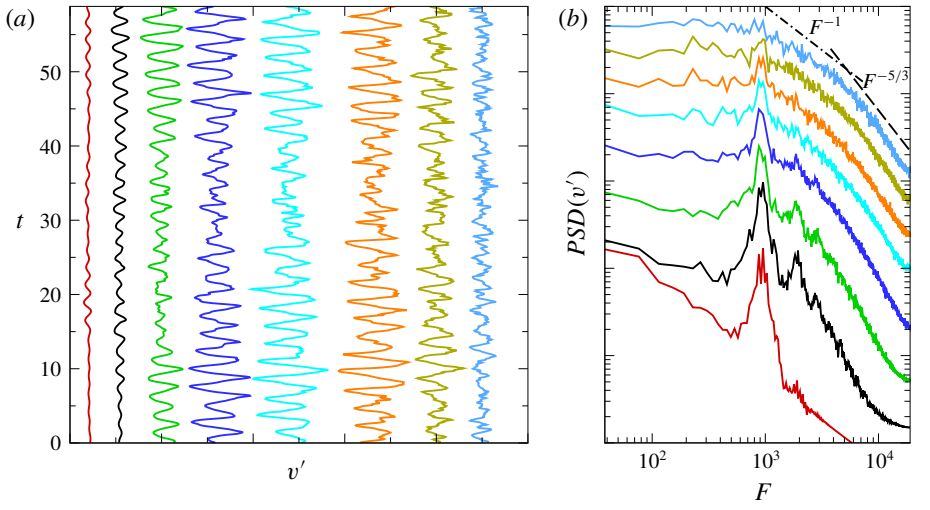

FIGURE 14. (Colour online) Temporal evolution (*a*) and the corresponding frequency spectra (*b*) of the wall-normal disturbance velocity (averaged in the spanwise direction) at various streamwise locations along the displacement thickness for zero FST simulation. Curves from left to right (bottom to top): $x = 8.5$, 9, 9.5, 10, 10.5, 11, 12 and 13.

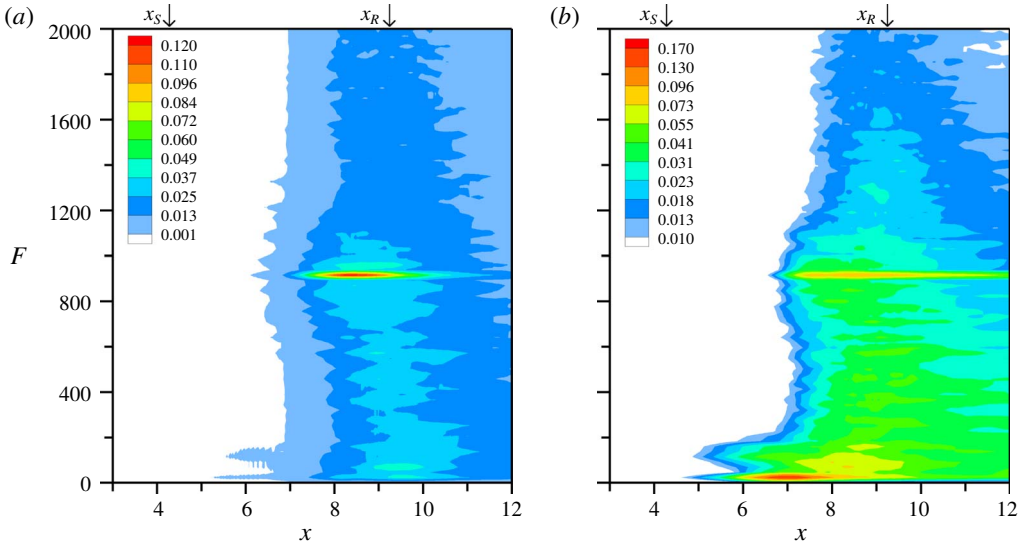

FIGURE 15. (Colour online) Spectral analysis for $Tu_0 = 0.5\,\%$. (*a*) Fourier spectra of the wall-normal disturbance velocity versus downstream direction along the displacement thickness. (*b*) Wall-normal maxima of Fourier amplitude of the streamwise disturbance velocity inside the boundary layer versus downstream direction.

amplitudes are extracted at $y = \delta^*(x)$. The dominant frequency, when the FST is included, remained close to the natural shedding frequency of the zero FST simulation, i.e. $F \approx 915$. However, as the level of FST increases, the frequency spectrum becomes broader and the 'dominant' frequency peak, although still identifiable in the spectra,

is less pronounced. This observation is consistent with the earlier experimental investigation of Burgmann & Schröder (2008), who found that the dominant shedding frequency of LSBs associated with the KH vortices are almost unaffected by the FST intensity (up to 1.5 %).

It is important to note that the results from the spectral analysis for the LSBs support the findings of Diwan & Ramesh (2009) that the non-dimensional dominant shedding frequency, $\overline{F}$, scales linearly with the modified Reynolds number, $\overline{R}$, in the linear regime. Here, $\overline{F} = Re f_{sh}(y_{in}^2 + \delta_\omega^2)$ and $\overline{R} = Re\, U_{in} y_{in}\sqrt{y_{in}/\delta_\omega}$, where f_{sh} is the most amplified frequency (shedding frequency), y_{in} is the wall-normal position of the inflection point, U_{in} is the mean streamwise velocity at the inflection point and δ_ω is the vorticity thickness (see Diwan & Ramesh 2009). In particular, for the LSBs without and with FST, $\overline{F} \approx 0.2\overline{R}$. It is worth noting that this scaling holds also in the APG region prior to the separation location, which further corroborates the conjecture by Diwan & Ramesh (2009) that the origin of the primary instability mechanism can be traced back to upstream of the separation location.

Note that the spectra shown in figure 15(*a*) were based on the wall-normal disturbance at the local displacement thickness away from the wall. As discussed in § 1.2, FST should give rise to so-called Klebanoff modes with their characteristic very low frequencies that should already be present in the approach boundary layer upstream of the separation. In figure 15(*a*) no such low-frequency peaks were observed. Thus, the question arises if the Klebanoff modes are suppressed in the presence of separation or if they were missed by using the wall-normal disturbance velocity at the (local) displacement thickness. To answer this question, the maximum amplitude of the disturbance u-velocity is now used instead. This is motivated by the fact that the primary mechanism of Klebanoff modes is a spanwise (low-frequency) modulation of the streamwise velocity component. Consequently, in figure 15(*b*) the (wall-normal) maximum amplitude of the u'-velocity is plotted in the F–x plane for the case with $Tu_0 = 0.5\,\%$. Now in addition to the dominant shedding frequency, $F \approx 915$, that was already found before, a much stronger peak appears near $F \approx 26$.

The frequency spectra now clearly indicate the generation of low-frequency disturbances, due to the presence of Klebanoff modes, which are strongly amplified downstream of the separation location. These low-frequency modes were analysed in the m–x plane spectra as shown in figure 16, where m is the spanwise mode number (e.g. $m = 1$ indicates that the spanwise width of the disturbances is $\lambda_z = L_z$ and for $m = 2$, $\lambda_z = L_z/2$, and so on). There is a dominant spanwise mode number $m = 5$ ($\lambda_z = L_z/5$) for which the disturbances have the maximum amplitude. This agrees very well with the instantaneous flow visualization (see figure 6). Another observation is that increasing FST levels caused higher K-mode amplitudes inside the boundary layer.

Corresponding to the results presented in figures 15 and 16, the spatial development of instability waves associated with the high-frequency 2D mode and low-frequency 3D mode are presented in figure 17 for $Tu_0 = 0.5\,\%$. Plotted are the Fourier amplitude of the u'-velocity together with the mean dividing streamline (dashed lines) and displacement thickness (solid line). Two important observations can be made from figure 17. The low-frequency 3D (K) mode is strongly amplified once embedded in the separated shear layer and exhibits a strong peak away from the wall. The maximum of the disturbance aligns with the displacement thickness and the maximum amplitude is reached in the front part of the bubble. On the other hand, the amplitude profile of the u'-velocity for 2D disturbances with the shedding frequency is composed of an inviscid shear layer instability and wall-mode instability where they can be

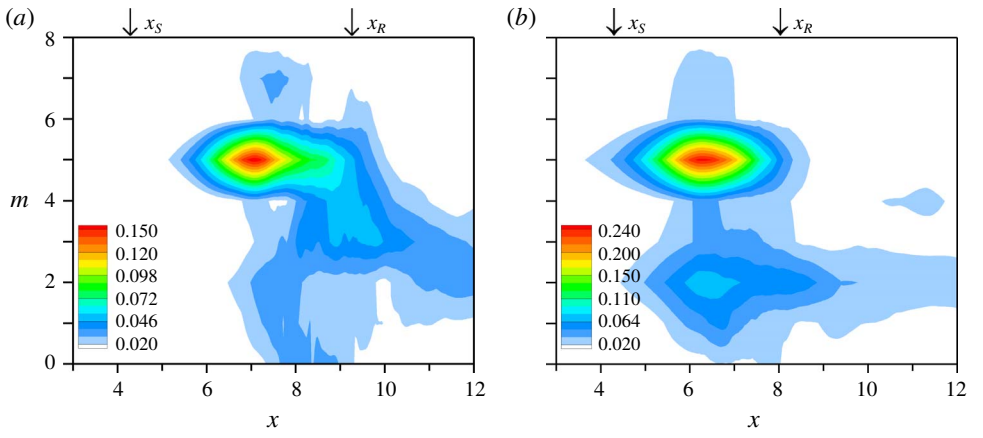

FIGURE 16. (Colour online) Contours of the maximum amplitude inside the boundary layer ($y < \delta$) of disturbance streamwise velocity in the spanwise mode number m–x spectrum for the frequency $F \approx 25$: (*a*) $Tu_0 = 0.5\,\%$, (*b*) $Tu_0 = 3\,\%$. The mean separation and reattachment locations are marked by down arrows.

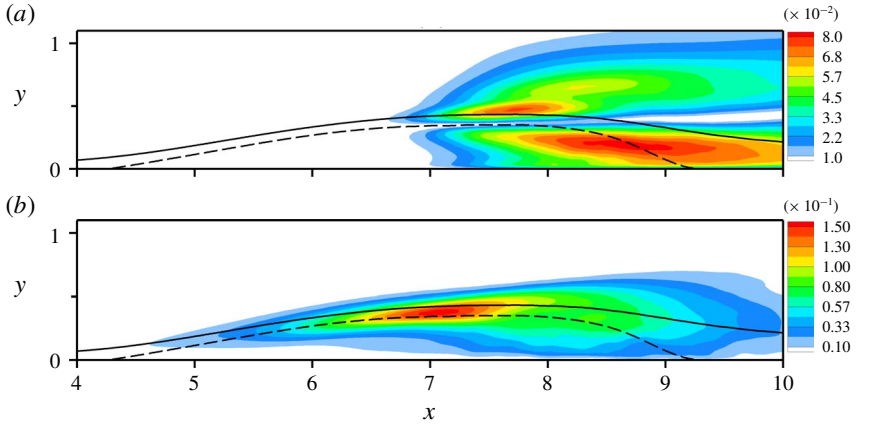

FIGURE 17. (Colour online) Contours of Fourier amplitude of streamwise velocity disturbance for $Tu_0 = 0.5\,\%$: (*a*) plotted at $F = 915$ and $m = 0$; (*b*) plotted at $F = 26$ and $m = 5$. Dashed line and solid line are time- and spanwise-averaged dividing streamline and displacement thickness, respectively.

distinguished by the streamwise position and the relative wall normal location of the maxima. While the former reaches the maximum at the maximum bubble height, the latter is confined to the wall in the region so-called reverse-flow vortex. This can be interpreted as being caused by the increasing wall shear in this region.

Thus, based on these observations, in the presence of FST two different instability modes can be identified in the laminar–turbulent transition process: (i) the strongly amplified 2D modes with a shedding frequency that is directly related to the KH instability, and (ii) the 3D low-frequency Klebanoff modes caused by the FST. To have a complete picture and assess the contributions of both identified instability mechanisms for different FST intensities, the evolution of the spectral disturbance

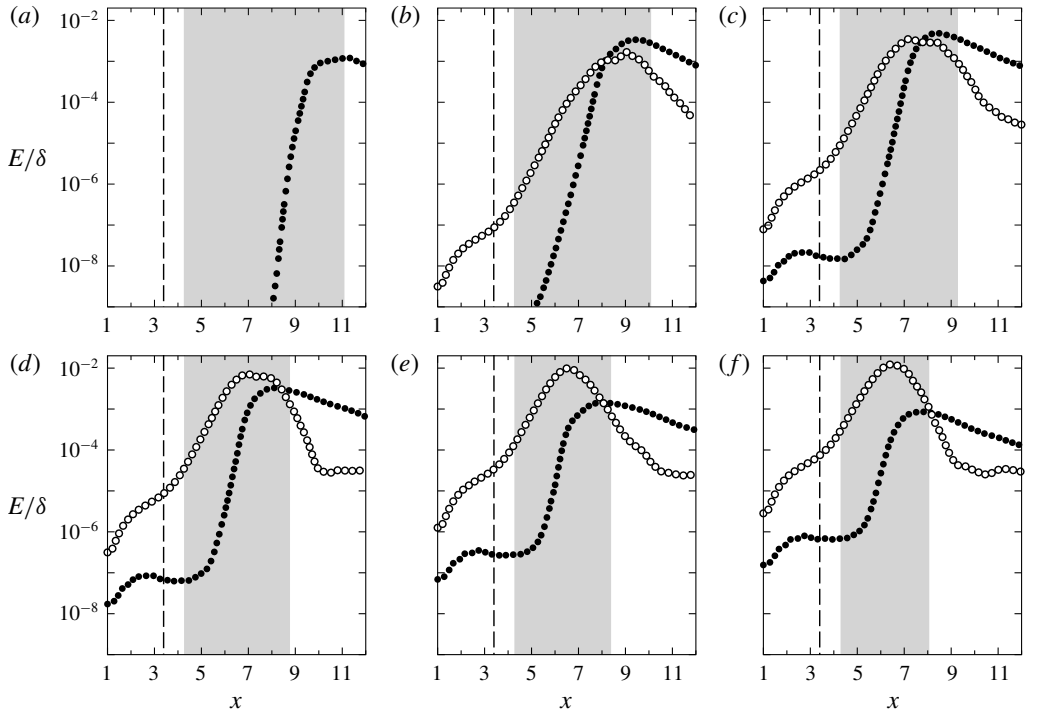

FIGURE 18. Comparison of the downstream development of spectral disturbance kinetic energy between the 2D modes at the fundamental frequency, (915, 0) (●), and the 3D low-frequency disturbances, (26, 5) (○): $Tu_0 = 0$ (*a*), 0.1 % (*b*), 0.5 % (*c*), 1 % (*d*), 2 % (*e*), and 3 % (*f*). The shaded area corresponds to the mean separation bubble and the onset of the APG is represented by dashed lines.

kinetic energy (SDKE) for each mode was tracked in the downstream direction in figure 18. The SDKE is computed from the wall-normal integral of the Fourier amplitude of the velocity components according to

$$E^{(F,m)}(x) = \frac{1}{2}\int_0^{\delta(x)} [u_A^{(F,m)}(x,y)^2 + v_A^{(F,m)}(x,y)^2 + w_A^{(F,m)}(x,y)^2]\,\mathrm{d}y, \tag{3.2}$$

where $\delta(x)$ is the local boundary-layer thickness. The notation (F, m) is used for a pair of mode numbers where F is the non-dimensional frequency (see (3.1)) and $2\pi m/L_z$ is the spanwise wavenumber of a structure. Therefore, mode (26, 5) corresponds to the Klebanoff modes and (915, 0) represents the 2D disturbances with the fundamental (shedding) frequency. In each of the six panels in figure 18, the mean separation region is indicated by the shaded area and the onset of the APG is denoted by dashed lines.

As the level of FST increases, the 2D and 3D disturbances in the attached laminar boundary layer exhibit higher amplitude levels where the K-mode has initially a much larger amplitude than the 2D mode. Immediately downstream of the inflow location, the K-mode experiences streamwise growth for $x < 1.8$, which is most likely the consequence of transient growth and lift-up mechanisms described in § 1.2. The initial transient growth of the K-mode is alleviated in the region of a strong favourable

pressure gradient $1.8 < x < 3.4$. Downstream of the APG, the K-mode experiences strong exponential growth until it saturates at a finite nonlinear amplitude. Based on this observation and the contours of the Klebanoff disturbances presented in figure 17, it can be conjectured that, once the K-mode is embedded within the separated region, it exhibits exponential growth instead of algebraic.

Just downstream of the inflow location the 2D mode also undergoes growth, but at a smaller rate compared to the K-mode. The growth could be attributed to the initial adjustment of the artificial inlet turbulence. After this initial phase, the 2D mode remains almost constant without experiencing significant downstream growth. Based on the linear stability analysis from our previous research (see Hosseinverdi *et al.* 2012), the location corresponding to Re_{cr} is between the onset of the APG and the separation location; however, exponential amplification of the 2D mode is initiated further downstream inside the separated region. It appears that the vortical fluctuations due to FST are not as effective in generating TS waves as in inducing the streamwise streaks. This observation can be explained by the so-called 'shear sheltering' phenomenon (Hunt *et al.* 1996; Jacobs & Durbin 1998), which describes the effect that the boundary layer acts as a low-pass filter, admitting predominantly low-frequency modes to penetrate into the boundary layer and sheltering the high-frequency range disturbances (like oscillations within the KH frequency range).

The maximum amplitude of the 2D mode slightly increases when the intensity of the FST is increased to $Tu_0 = 0.5\,\%$. When the FST level is increased further, the maximum amplitude of the 2D mode starts to decrease. On the other hand, higher FST intensity promotes stronger Klebanoff modes. In addition to the disturbance kinetic energy level, 2D KH modes can be distinguished from the K-mode by their exponential growth rate, i.e. larger growth rate for 2D mode. One would expect that, with increasing FST, the dominant structures would lose their spanwise coherence as observed in figure 7 for example. In conclusion, for the lowest level of FST, $Tu_0 = 0.1\,\%$, the region upstream of the reattachment location, which is at the end of the transition region, is dominated by 2D modes, while for the high levels of FST, $Tu_0 = 2\,\%$ and $Tu_0 = 3\,\%$, the Klebanoff modes are dominant in the entire transition region. For the FST levels in between $0.1\,\%$ and $2\,\%$, the two modes are blended together and contribute to the transition process simultaneously. Downstream of the mean reattachment location, the K-modes are decaying much faster than the 2D modes and thus 2D waves exhibit larger amplitudes.

3.4. *Modal decomposition*

The detection of dominant vortical flow structures is important since the topology of the fluid motion is closely related to the dynamics of these structures. A transitional flow often consists of a superposition of flow structures with different dominant frequencies and wavelengths. However, the instantaneous flow structures, as shown in figure 6 for example, do not provide a complete understanding regarding the underlying flow physics. Therefore, a detailed analysis of the simulation data using modal decomposition is carried out to provide additional insight into the underlying flow physics for various FST intensities. In particular, proper orthogonal decomposition and dynamic mode decomposition have been carried out to identify dominant structures and dynamics of the evolving flow within the transition region as a consequence of hydrodynamic instabilities.

Proper orthogonal decomposition (POD), first proposed by Lumley (1967) in the field of fluid mechanics, is a method for identifying large-scale energetic flow

structures in transitional and turbulent flows. For the present results, the snapshot method that was proposed by Sirovich (1987) is employed. In the POD method, for a given set of time- (t) and space-dependent ($\boldsymbol{x}$) flow data, the flow field can be represented by

$$\boldsymbol{u}(\boldsymbol{x}, t_n) = \sum_{i=0}^{N-1} a_i(t_n)\boldsymbol{\phi}_i(\boldsymbol{x}), \tag{3.3}$$

where the $\boldsymbol{\phi}_i$ are the POD spatial eigenfunctions and the a_i are the POD time coefficients. The POD modes are orthogonal and optimized with respect to their energy content, i.e. the largest fraction of the total kinetic energy of the flow field is captured with the smallest number of modes. Therefore, assuming that large-scale coherent structures possess a significant amount of energy, POD can provide valuable information regarding the most relevant flow structures.

The dynamic mode decomposition (DMD), proposed by Schmid (2010), is a data-driven technique capable of extracting dynamical information from data sequences obtained from DNS or experiments. The DMD decomposition allows for an expansion of the velocity data in the form

$$\boldsymbol{u}(\boldsymbol{x}, t_n) = \sum_{j=0}^{N-1} \mu_j^n \boldsymbol{\psi}_j(\boldsymbol{x}), \tag{3.4}$$

where the $\boldsymbol{\psi}_j$ are the complex-valued spatial DMD modes and the μ_j are called the Ritz eigenvalues associated with the respective DMD mode. It should be noted that the μ_j are complex-valued, giving each mode a corresponding growth rate σ_j and oscillatory angular frequency ω_j as follows:

$$\mu_j^n = \mathrm{e}^{(\sigma_j + \mathrm{i}\omega_j)t/\Delta t}, \quad \sigma_j = \frac{1}{\Delta t}\log|\mu_j|, \quad \omega_j = \frac{1}{\Delta t}\,a\tan\left(\frac{\mathcal{I}(\mu_j)}{\mathcal{R}(\mu_j)}\right), \tag{3.5a–c}$$

where Δt is the time interval between two consecutive snapshots. In contrast to POD, where a spatial orthogonality of the eigenfunctions could lead to a broad range of frequencies for each individual POD mode, DMD extracts coherent structures with a single frequency. For details of DMD, see Schmid (2010).

For the present modal decomposition analysis, 720 snapshots of the velocity field $(u, v, w)^{\mathrm{T}}$ equidistantly distributed over 18 fundamental (shedding) periods are used. The focus here is on identifying and extracting the dominant and coherent structures in the transitional region from the initial linear stage up to the nonlinear development of the instability waves. Therefore, the spatial extent of the snapshots was chosen from $x = 3$ (upstream of the separation location) up to the mean reattachment location for each case. The POD energy spectrum for the zero FST case and the cases with 0.5 %, 1 % and 3 % of FST intensity are shown in figure 19. The left vertical axis represents the fraction of energy, E_i, and the right vertical axis indicates the cumulative energy sum, S_p, which are defined as

$$E_i = \left(\lambda_i \Big/ \sum_{j=1}^{N-1}\lambda_j\right) \times 100, \quad S_p = \left(\sum_{i=1}^{p}\lambda_i \Big/ \sum_{j=1}^{N-1}\lambda_j\right) \times 100. \tag{3.6a,b}$$

In the above equations, λ_i is the magnitude of the eigenvalue of the POD mode, which corresponds to twice the kinetic energy content of the respective POD mode,

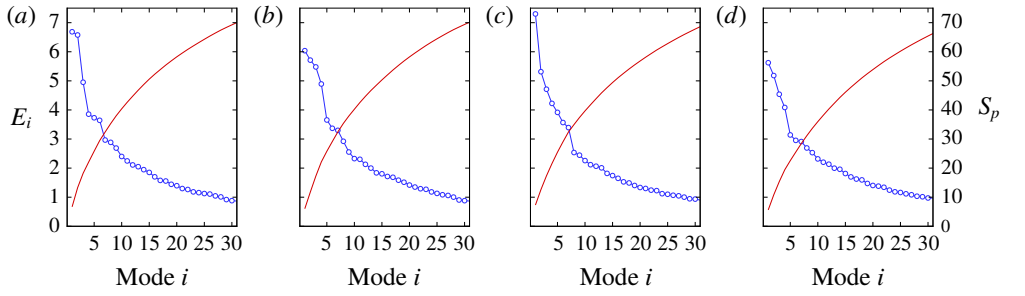

FIGURE 19. (Colour online) Relative (left axis) and cumulative (right axis) POD eigenvalues (energy) spectrum distribution: (*a*) $Tu_0 = 0$; (*b*) $Tu_0 = 0.5\,\%$; (*c*) $Tu_0 = 1\,\%$; and (*d*) $Tu_0 = 3\,\%$.

and N is the total number of POD modes. Since the mean flow was not subtracted from the flow field prior to the decomposition, the zeroth POD mode, which represents the mean flow and therefore contains most of the kinetic energy, is not considered here. Thus, the presented E_i and S_p correspond to the unsteady POD modes.

The POD eigenvalue spectra, shown in figure 19, reveal that, for all cases, most of the energy is contained in the lower mode numbers, although the distribution of energy among the modes is different for the investigated cases. In particular, for the zero FST simulation and the case with $Tu_0 = 0.5\,\%$, the most energetic modes (modes 1 and 2) have almost identical magnitudes. For the other cases ($Tu_0 = 1\,\%$–$3\,\%$), however, the energy drops among the dominant modes. The drop-off rate in the magnitude of the eigenvalues with respect to the higher mode numbers is similar for all cases. Furthermore, figure 19 indicates that approximately 4.2 % of the unsteady modes (30 modes) only are needed to reproduce 70 % of the unsteady kinetic energy. In the following, the eigenfunctions of the 'most energetic' POD modes, their respective time coefficients and the associated Fourier spectra of the time coefficients, and the most coherent dynamic modes and their corresponding growth rates and frequencies are inspected in detail for different levels of FST. The POD and DMD modes are visualized by isosurfaces of the u/v velocity component. Here, time is non-dimensionalized by the shedding period, $t_{nd} = t/t_{sh}$, and similarly the frequency is non-dimensionalized by the shedding frequency, $f_{nd} = f/f_{sh}$.

Figure 20 demonstrates that the dominant POD modes exhibit large spanwise-oriented structures for the case without FST. The phase shift in modes 1 and 2 indicates that these modes form pairs, which physically represent structures that are travelling in the streamwise direction ('travelling waves'). It can therefore be concluded that the spatially evolving coherent structures, $\gamma(\boldsymbol{x}, t)$, are represented by pairs of eigenfunctions according to $\gamma(\boldsymbol{x}, t) = a_1(t)\boldsymbol{\phi}_1(\boldsymbol{x}) + a_2(t)\boldsymbol{\phi}_2(\boldsymbol{x})$. Detailed inspection of modes 1 and 2 also reveals that these modes are composed of 2D and oblique structures. This observation led to the conjecture that the amplification of weakly oblique 3D disturbances due to the inviscid shear-layer instability mechanism may lead to the formation of oblique coherent structures. The time signals of modes 1 and 2 exhibit nearly sinusoidal behaviour with a dominant frequency matching the shedding frequency, $f_{nd} = 1$, as shown in figure 21. It is worth noting that there is a narrow band around the dominant frequency which could be related to the composite structures of modes 1 and 2. POD mode 3 is oriented in the streamwise direction with the preferred spanwise wavelength $\lambda_z \approx L_z/3$. The corresponding time signal

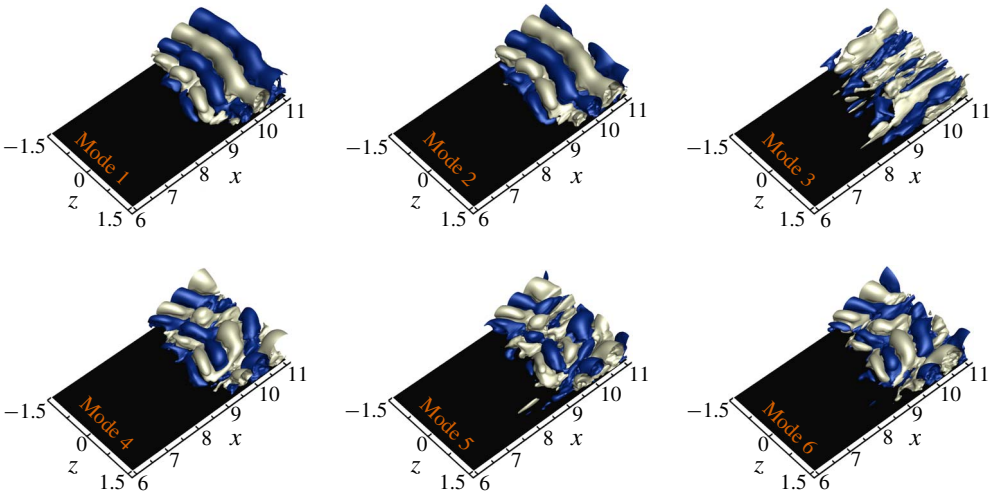

FIGURE 20. (Colour online) Dominant POD eigenfunctions for the zero FST case. Shown are positive (light grey) and negative (blue) isosurfaces of $|v| = 0.1$.

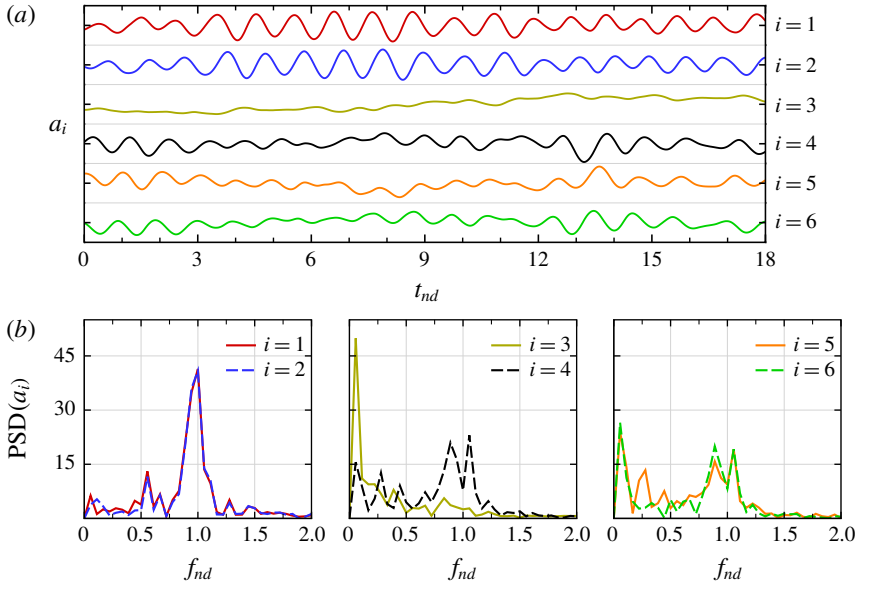

FIGURE 21. (Colour online) (*a*) POD time coefficients and (*b*) associated frequency spectra for the zero FST case.

of this mode has a very long period (low-frequency content). The 3D structures with spanwise wavelength $\lambda_z = L_z$ are identified by modes 4–6. The frequency spectra associated with these modes show two dominant frequency bands close to the shedding frequency, $f_{nd} = 0.9$ and 1.06.

To gain further insight into the coherent structure dynamics, the four least damped DMD modes are illustrated in figure 22. DMD modes 1 and 2 capture purely oblique and 2D structures, respectively. The composite structures (2D and oblique structures)

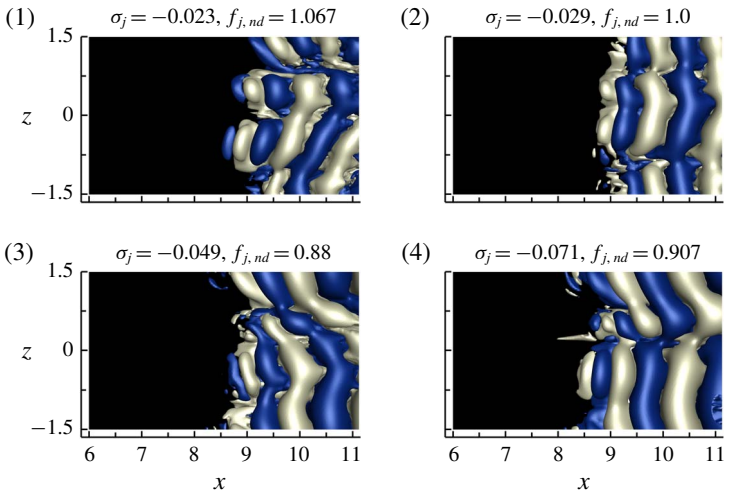

FIGURE 22. (Colour online) DMD eigenfunctions for the case with zero FST. Here σ_j and f_j are the corresponding growth rate and frequency, respectively. Shown are isosurfaces of $|v| = 0.01$.

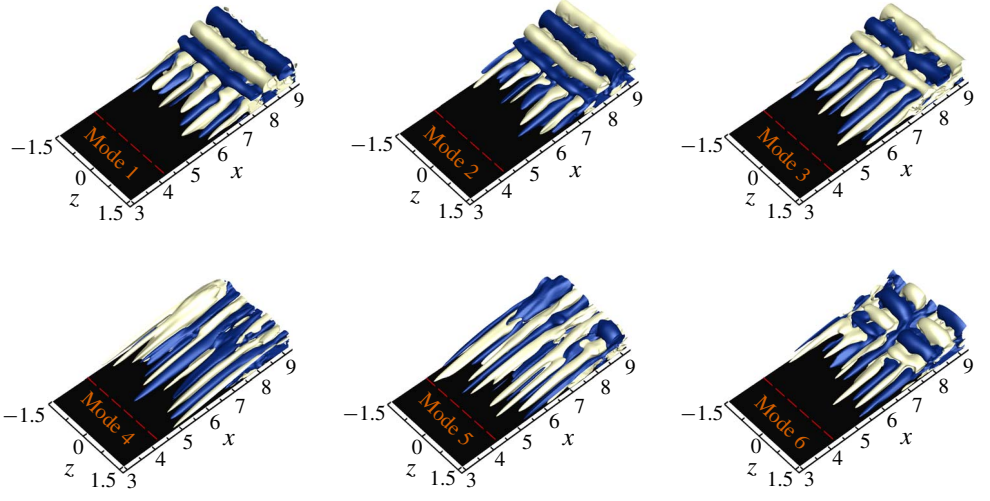

FIGURE 23. (Colour online) POD eigenfunctions for the case $Tu_0 = 0.5\,\%$. Shown are positive (light grey) and negative (blue) isosurfaces of $|u| = 0.08$. Dashed lines indicate the mean separation location.

are identified by modes 3 and 4. Another interesting observation is that the oblique structures (mode 1) are more unstable than 2D disturbances (mode 2).

From the 3D visualizations of POD modes 1, 2 and 3 for $Tu_0 = 0.5\,\%$ shown in figure 23, two different flow structures can be identified: (i) spanwise structures (2D) as the result of the KH instability mechanism and (ii) 'streaky' structures which correspond to the Klebanoff modes caused by FST. In particular, the dominant structures (modes 1, 2 and 3) have initially a streaky pattern, with alternating positive and negative streamwise velocity fluctuations, that later turns into a 2D structure.

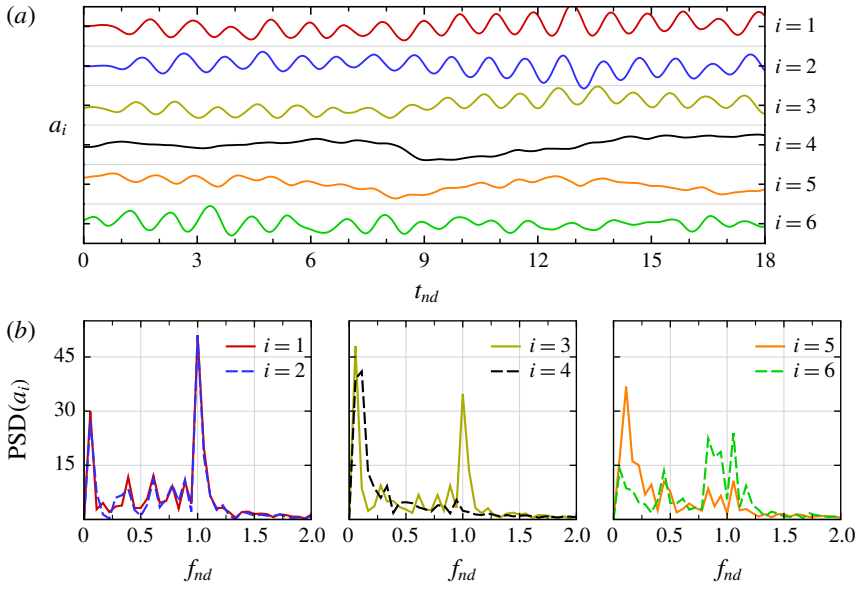

FIGURE 24. (Colour online) (*a*) POD time coefficients and (*b*) respective frequency spectra for the case $Tu_0 = 0.5\,\%$.

The spanwise wavelength of the Klebanoff modes is in agreement with the results from instantaneous visualizations and spectral analysis ($\lambda_{z,K} \approx L_z/5$). Accordingly, the frequency spectra associated with these modes provided in figure 24 show two dominant frequency bands: the high-frequency spectral peak is related to the spanwise structures while the low-frequency peak corresponds to Klebanoff modes. Although the shedding frequency amplitude (high-frequency peak) for modes 1 and 2 is larger than the low-frequency peak amplitude (Klebanoff mode), the opposite is true for mode 3. POD modes 4 and 5 display purely low-frequency streamwise-oriented 'streaky' structures. However, the frequency and spanwise spacing are different from those captured by modes 1–3. The structures with chequerboard pattern with $\lambda_z = L_z$ in mode 6 in figure 23 have almost the same dominant frequency as POD modes 4–6 for the zero FST case.

The DMD method is able to capture the dominant modes related to the KH and Klebanoff modes separately as illustrated in figure 25. Unsteady 'streaky' and steady structures are identified by DMD modes 3 and 4 in figure 25, which shows that the steady mode is highly damped. In contrast to the zero FST simulation, the 2D structure with the shedding frequency is the most unstable mode among the high-frequency disturbances. POD and DMD investigations for $Tu_0 = 0.5\,\%$ support the fact that 2D disturbances within the flow with frequency close to the KH frequency range are the most amplified instability waves in the presence of a finite low-amplitude disturbance environment.

Figure 26 demonstrates that the transition region is dominated by the K-mode for the case with $Tu_0 = 1\,\%$ as captured by the dominant POD mode (cf. mode 1). A similar shape is observed in mode 2; however, the appearance of spanwise structures occurs further downstream. The drop in the magnitude of the eigenvalues between modes 1 and 2 as observed in figure 19(*c*) could be explained by the fact that modes 1 and 2 do not represent travelling pairs, and therefore they do not occupy the same

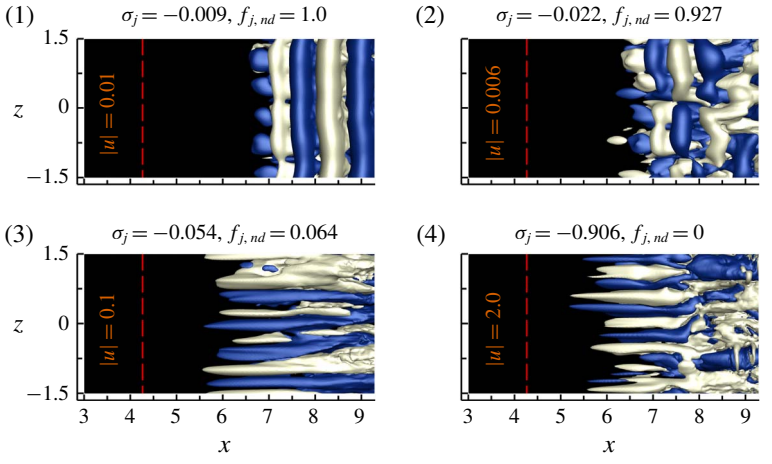

FIGURE 25. (Colour online) DMD eigenfunctions for the case $Tu_0 = 0.5\,\%$. Here σ_j and f_j are the corresponding growth rate and frequency, respectively. Dashed lines indicate the mean separation location.

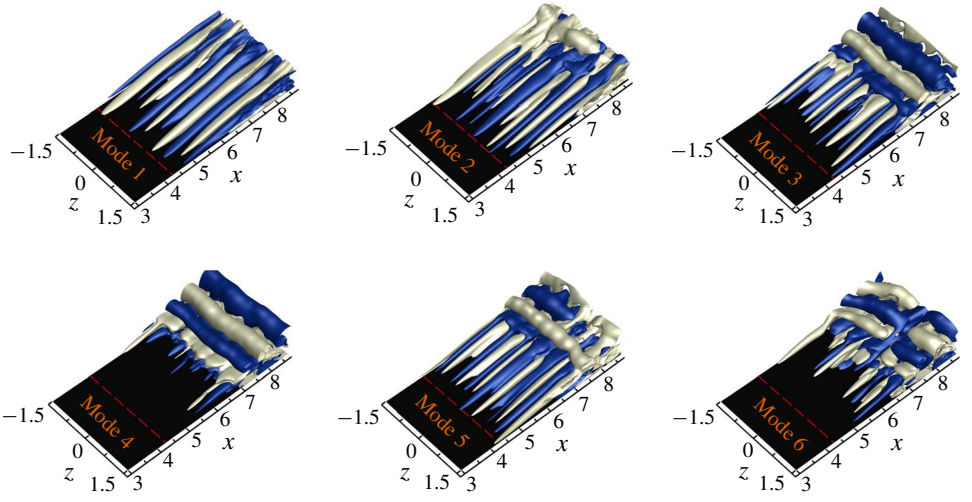

FIGURE 26. (Colour online) POD eigenfunctions for the case $Tu_0 = 1\,\%$. Shown are positive (light grey) and negative (blue) isosurfaces of $|u| = 0.08$. Dashed lines indicate the mean separation location.

energy level as was the case for zero FST and $Tu_0 = 0.5\,\%$. Fully developed KH structures are present in the higher modes 3–5 and the chequerboard pattern can be observed in mode 6.

This detailed analysis based on modal decomposition supports the results obtained from the spectral analysis that the low-frequency 3D Klebanoff modes and high-frequency 2D disturbances are blended together and contribute to the transition process for cases with the FST intensities of $Tu_0 = 0.5\,\%$ and $Tu_0 = 1\,\%$. Whereas the large contribution comes from the KH instability mechanism for the $Tu_0 = 0.5\,\%$ case, the Klebanoff modes play a more dominant role in the $Tu_0 = 1\,\%$ case.

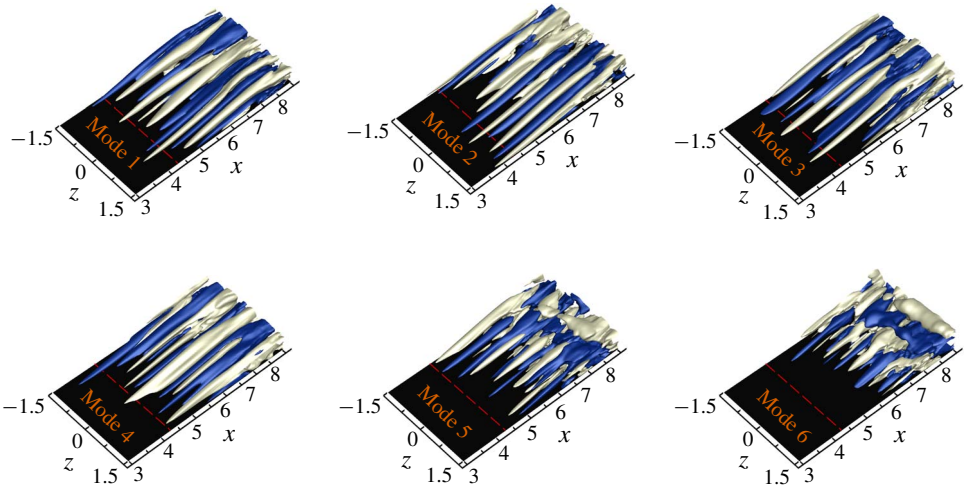

FIGURE 27. (Colour online) POD eigenfunctions for the case $Tu_0 = 3\,\%$. Shown are positive (light grey) and negative (blue) isosurfaces of $|u| = 0.2$. Dashed lines indicate the mean separation location.

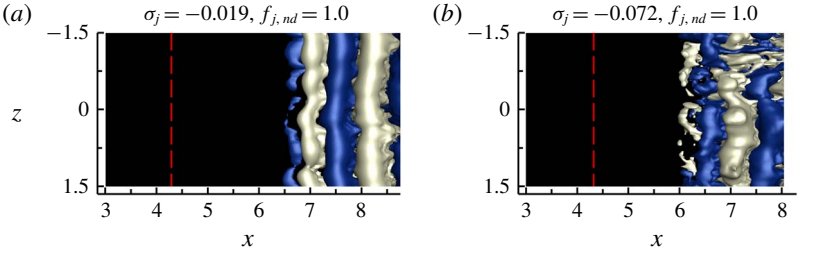

FIGURE 28. (Colour online) DMD eigenfunctions for the 2D mode: (*a*) $Tu_0 = 1\,\%$ and (*b*) $Tu_0 = 3\,\%$.

The perspective views for the streamwise velocity component in figure 27, for the highest level of FST intensity investigated here ($Tu_0 = 3\,\%$), demonstrate that the most energetic structures are streamwise streaks with a distinct spanwise wavelength. Evidence of spanwise structures is only visible in modes 5 and 6, although they are not fully developed. Finally, figure 28 compares the 2D structures with the shedding frequency obtained from DMD for $Tu_0 = 1\,\%$ and $Tu_0 = 3\,\%$.

3.5. *Linear inviscid instability: linearized Navier–Stokes equations*

The results presented thus far indicate that the K-modes dominate the transition region for $Tu_0 > 1\,\%$. Of particular importance is the observation that the slow streamwise growth of the K-mode was overtaken by much stronger amplification rate downstream of the onset of the APG as the K-mode exhibits exponential growth in the strong APG region. To further corroborate this observation, a linear instability investigation with respect to the low-frequency 3D disturbances was carried out.

To predict the evolution of instabilities in the linear regime, we developed an approach that directly solves the linearized Navier–Stokes equations (LNSE) without

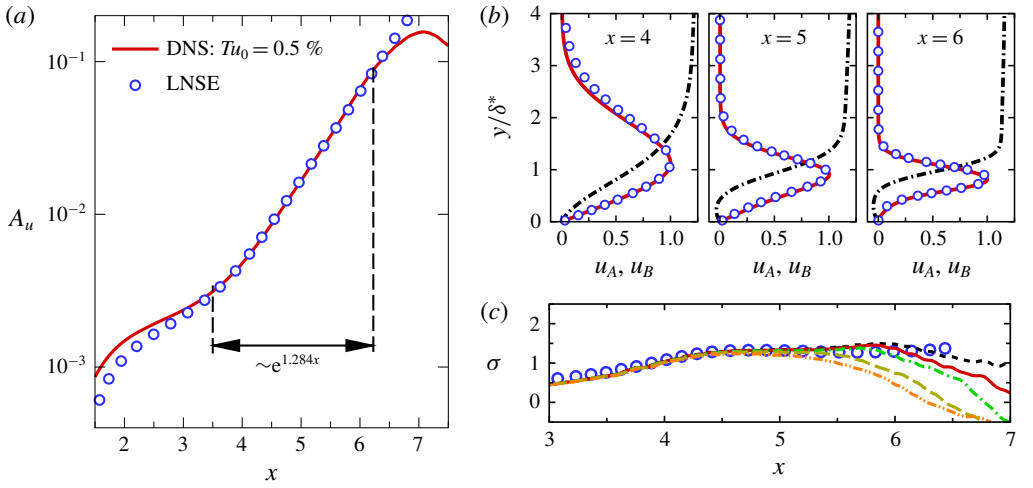

FIGURE 29. (Colour online) (*a*) Streamwise development of K-mode, mode (26, 5), computed with LNSE and DNS with $Tu_0 = 0.5\,\%$. (*b*) Wall-normal distributions of the u'-velocity Fourier amplitudes at several x-locations obtained from LNSE and DNS with $Tu_0 = 0.5\,\%$ for mode (26, 5). Disturbance amplitudes are scaled by their respective maxima and dash-dotted lines represent the corresponding time-averaged u-velocity profile (u_B). Wall-normal coordinates are normalized by the local mean displacement thickness. (*c*) Comparison of local spatial growth rates obtained from LNSE and DNS with $Tu_0 = 0.1\,\%$ (– – –), $0.5\,\%$ (——), $1\,\%$ (–·–·), $2\,\%$ (– – –) and $3\,\%$ (–···–···).

using any additional assumptions as required by linear stability theory (LST), i.e. assuming that basic flow is parallel (parallel flow assumption). Thus, all locally non-parallel effects of the basic flow are included in the LNSE approach, which is important as separated flows are considered here. For the linear instability analysis employed here based on LNSE, the total flow field is decomposed into the base flow (or basic flow) $\boldsymbol{u}_B(x, y)$ and $\boldsymbol{\omega}_B(x, y)$ and disturbances $\boldsymbol{u}'(\boldsymbol{x}, t)$ and $\boldsymbol{\omega}'(\boldsymbol{x}, t)$. Substituting these decompositions into the Navier–Stokes equations (2.1) yields the governing equations for the total flow field, which after linearization (by neglecting products of the disturbance quantities) is a linear superposition of the base flow and the disturbance flow. Thus, the governing equations for the base flow can be subtracted from the equations for the total flow in order to obtain the LNSE. For numerically solving the LNSE, the same time integration and spatial discretization schemes are employed as for the nonlinear equations used in the DNS.

For generating streamwise vortices outside the boundary layer in the LNSE solver in order to excite Klebanoff modes inside the boundary layer (for example mode (26, 5), which is associated with the K-mode), an unsteady volume force is used as a source term on the right-hand side of the LNSE. For more details regarding this approach, see Fasel (2002) and Hosseinverdi & Fasel (2018). In figure 29, the downstream development of the wall-normal maximum of the u'-velocity Fourier amplitude (A_u) and the u'-velocity Fourier amplitude profile (u_A) of the 3D disturbance wave with the spanwise mode number $m = 5$ (which corresponds to the lateral wavelength of the K-mode) are plotted as obtained from the LNSE and are compared with the DNS results of an LSB with $Tu_0 = 0.5\,\%$. For the base flow used in the LNSE investigation, the time- and spanwise-averaged results obtained for $Tu_0 = 0.5\,\%$ are employed.

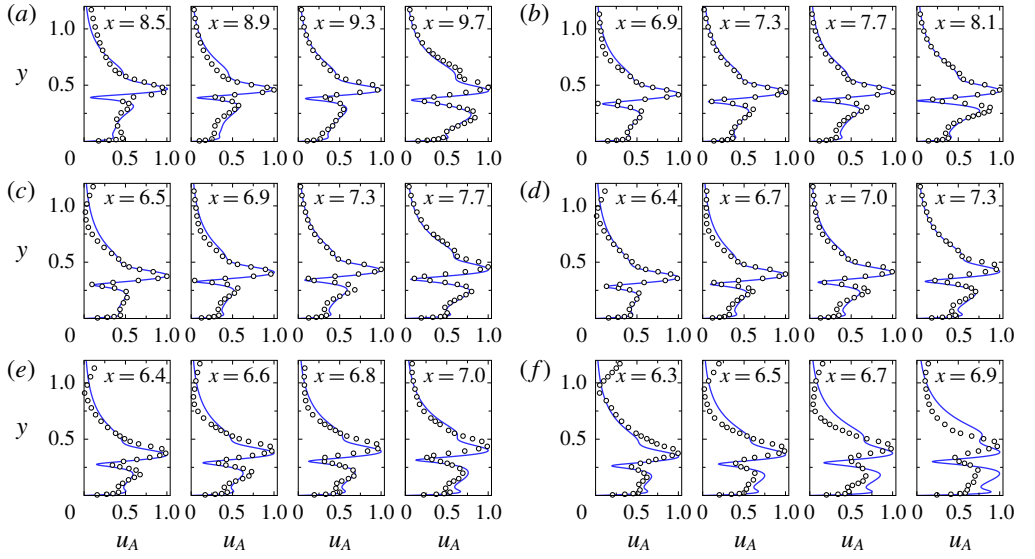

FIGURE 30. (Colour online) Comparison of wall-normal distribution of u'-velocity Fourier amplitudes obtained from LNSE (——) and DNS (○) for 2D disturbances with shedding frequency: (*a*) $Tu_0 = 0$, (*b*) $Tu_0 = 0.1\,\%$, (*c*) $Tu_0 = 0.5\,\%$, (*d*) $Tu_0 = 1\,\%$, (*e*) $Tu_0 = 2\,\%$, (*f*) $Tu_0 = 3\,\%$. Disturbance amplitudes are scaled by their respective maximum value.

In figure 29(*b*), the Fourier amplitudes are scaled by their respective maximum amplitudes and u_B is the corresponding time-averaged u-velocity profile. The streamwise evolution of the K-modes obtained from the LNSE compares very well with those from the DNS as shown figure 29(*a*). Of particular interest in figure 29(*a*) is that the K-mode indeed grows exponentially in the APG region ($A_u \sim \mathrm{e}^{1.284x}$). The comparison of the wall-normal distributions of the disturbance amplitude in figure 29(*b*) further confirms the proper implementation and accuracy of the LNSE method. The spatial growth rates associated with the K-mode as obtained from the LNSE (with the base flow corresponding to $Tu_0 = 0.5\,\%$) and DNS with various FST intensities are presented in figure 29(*c*). The local growth rate is computed based on the wall-normal maxima of u_A according to $\sigma(x) = \partial \log(u_{A,max})/\partial x$.

It is well known that, for attached boundary layers, the linear stages of the transition process are bypassed when FST intensity exceeds 1 % (Morkovin 1969; Jacobs & Durbin 2001; Matsubara & Alfredsson 2001). The critical FST intensity beyond which 'bypass' transition occurs depends of course on the pressure gradient, on the background spectrum of the perturbations and on the receptivity (Abu-Ghannam & Shaw 1980). Previous research (Greenblatt & Wygnanski 2000; Yarusevych, Kawall & Sullivan 2006; Marxen & Henningson 2011; Postl *et al.* 2011) has shown that an effective and efficient laminar separation control is achieved when a linear inviscid shear-layer instability is exploited. Therefore, it is necessary to examine the existence of a linear inviscid instability mechanism for different levels of FST. Next, the hydrodynamic instability with respect to 2D disturbances with the dominant frequency (shedding frequency) found in the spectral analysis as discussed in § 3.3 is investigated for different FST intensities. For each FST intensity, the corresponding time- and spanwise-averaged results obtained from the DNS is used as the base flow. Figure 30 compares the wall-normal Fourier amplitude distributions of the u'-velocity

between the DNS and the LNSE results for all cases. The amplitude distributions from both LNSE and DNS are normalized by their respective maximum value within the boundary layer. These profiles were extracted from the region of exponential growth up to the saturation location. The amplitude distribution from the DNS data agrees remarkably well with that obtained from LNSE for zero FST simulation and cases with $Tu_0 \leqslant 2\,\%$ even at the location where the disturbances saturate. For the highest level of FST, $Tu_0 = 3\,\%$, despite the good agreement at the beginning ($x = 6.3$), there are differences in the wall-normal location of the disturbance peaks and the amplitudes near the wall for profiles $x > 6.3$. The good agreement for the cases with $Tu_0 \leqslant 2\,\%$ confirms that 2D disturbances grow due to the linear, inviscid shear-layer instability mechanism, and that the primary linear stage of the transition process is not bypassed. As a result, unsteady flow control strategies may still be effective means to reduce/prevent separation for these cases by exploiting the inviscid shear-layer instability.

These findings are consistent with those by Balzer & Fasel (2016). It is important to note, however, that disturbances associated with the K-modes are orders of magnitude larger than the 2D KH instability waves for LSBs for high levels of FST, as demonstrated in the present investigations by spectral analysis and POD. Hence, it is postulated that, whereas a significant reduction of the separation length can be obtained with unsteady flow control techniques, which are aimed at exploiting the shear-layer instability for zero and small levels of FST, laminar separation control becomes less effective for high levels of FST. Although flow control will exponentially amplify 2D modes, disturbances due to FST (K-modes) will remain at much larger amplitude levels compared to the 2D disturbances in the entire transition region. Thus, for higher levels of FST, in addition to exploiting the shear-layer instability, an effective and efficient active flow control is required also to reduce the streamwise growth of K-modes.

3.6. *Effect of free-stream turbulence energy spectrum*

For all cases, the von Kármán energy spectrum is used to distribute the turbulent kinetic energy among the modes with different wavenumbers (see § 2.5). A set of numerical simulations were performed while varying the energy spectrum of the incoming synthetic turbulence to investigate if and how it affects the transition process in LSB. Towards this end, energy spectra proposed by Ossia & Lesieur (2001) were employed,

$$E(k) = \frac{1}{2} Tu_0^2 \frac{A_s}{k_e} \left(\frac{k}{k_s}\right)^s \exp\left(-\frac{s}{2}\frac{k^2}{k_e^2}\right), \tag{3.7}$$

where A_s is a normalization constant chosen such that $\int E(k)\,\mathrm{d}k = 1.5 Tu_0^2$. The wavenumber k_e denotes the wavenumber of the most energetic structures ($k_e \approx 1.157/L_{11}$). The parameter s determines the slope of the low-wavenumber range. Figure 31 compares the typical spectrum obtained from the von Kármán energy spectrum (vKES) with that obtained using (3.7) with $s = 0.5$. The Ossia and Lesieur energy spectrum (OLES) decreases rapidly above a prescribed wavenumber k_e.

Simulations using the two different energy spectra, namely vKES and OLES, for the FST intensity of $Tu_0 = 0.1\,\%$ and $Tu_0 = 2\,\%$ were carried out. However, the results for $Tu_0 = 0.1\,\%$ are not reported here since the results obtained from the two spectra were very similar, so only the results for $Tu_0 = 2\,\%$ are discussed below. It should be noted that the wavenumber associated with the maximum energy and the integral

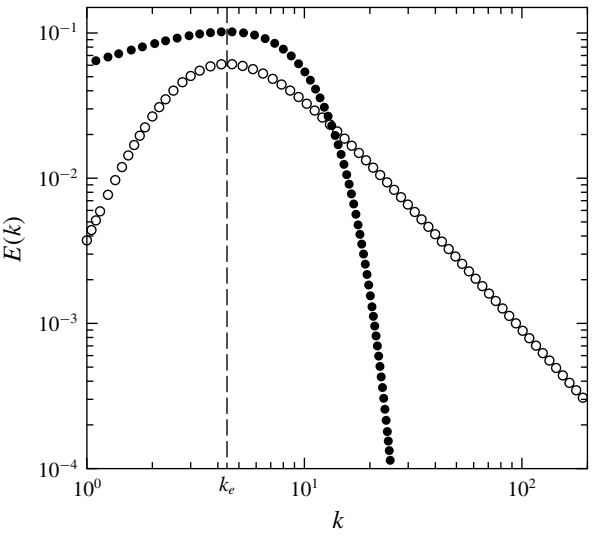

FIGURE 31. Energy spectra used to generate isotropic FST at the inflow boundary: ○, von Kármán energy spectrum, equation (2.5); ●, spectrum proposed by Ossia & Lesieur (2001), equation (3.7). The wavenumber of the maximum energy, k_e, is represented by the dashed line.

of the energy with respect to the wavenumber ($\int E(k)\,\mathrm{d}k$) are kept the same for both spectra.

Contours of spanwise, one-dimensional power spectra of the streamwise velocity component as a function of the spanwise mode number (m) are plotted for selected streamwise locations for the two FST spectra in figure 32. The spectra were computed using a spanwise Fourier transform and the relationship

$$E_{uu}(x, y, m) = \overline{u^m(x, y, t)u^m(x, y, t)}, \tag{3.8}$$

where the overbar indicates a time average and u^m symbolizes the Fourier-transformed u-velocity component in the spanwise direction (spanwise mode number m). Five x-stations were selected: the inflow boundary, x_{inlet}, the onset of the APG, x_{APG}, the separation location, x_S, the location of maximum bubble height, $x_{h,max}$, and the mean reattachment location, x_R. The wall-normal coordinate is normalized by the local boundary-layer thickness and the local displacement thickness is indicated by dashed lines in each panel.

For both cases, the energy in the power spectrum at the inflow is clearly concentrated in the free stream and the maximum amplitude is at $1 \leqslant m \leqslant 2$ (this is related to the chosen turbulent integral length scale L_{11}). While propagating in the downstream direction, the vortical structures in the free stream enter the boundary layer, as can be clearly observed at x_{APG}. At the onset of the APG, two bands ($m = 2$, $m = 5$) are visible for the case with vKES. The maximum amplitude has a spanwise mode number of $m = 5$, which, as already known from spectral analysis, corresponds to the K-mode. For the other case (OLES), however, the spectra are dominated by the disturbances with spanwise mode number of $m = 2$ without the appearance of the K-mode (or the K-mode has a smaller amplitude than minimum contour level). Moving further downstream to the separation location, the disturbances are amplified

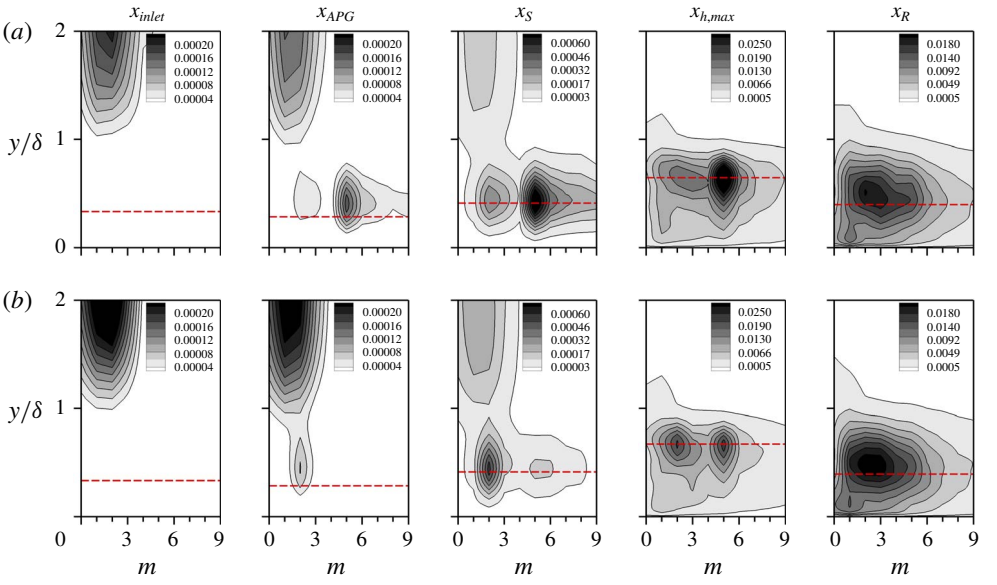

FIGURE 32. (Colour online) Contours of spanwise one-dimensional energy spectra of the streamwise velocity at selected streamwise locations obtained for (*a*) von Kármán energy spectrum and (*b*) Ossia and Lesieur energy spectrum. The wall-normal direction is scaled by the local boundary-layer thickness. The displacement thickness is marked by dashed red lines.

inside the boundary layer, and the trace of the K-mode becomes visible for the case with OLES although the disturbances with $m = 2$ are still dominant. Close to the location of maximum bubble height, the K-mode attains a larger amplitude than disturbances with a smaller wavenumber for the case with OLES. For the vKES case, the K-mode remains dominant and the disturbances with a smaller wavenumber have penetrated the boundary layer, which is more pronounced at the reattachment location where the near-wall peaks appear for a lower spanwise mode number, indicating that the boundary layer is starting to redevelop. The case OLES exhibits a similar pattern at the reattachment location.

A closer inspection of (3.7) and figure 31 reveals that the kinetic energy is distributed among the different modes such that the lower-wavenumber modes contain most of the kinetic energy and the spectrum lacks the high-wavenumber contents present in the von Kármán energy spectrum. This kind of distribution biases the energy distribution initially towards the low-wavenumber disturbances. However, the modes with low frequency and higher spanwise wavenumber (K-modes) become visible further downstream. Therefore, it could be speculated that, in the absence of high-wavenumber scales in the FST spectrum, the Klebanoff modes need a larger downstream distance to become dominant.

Figure 33 shows the downstream development of the SDKE and the energy growth ratio, $E(x)/E(x = 1)$, of the 2D modes with the fundamental frequency and of the low-frequency Klebanoff modes, mode (26, 5), obtained for the two different FST energy spectra. For the 2D modes, both cases experience the same amplification rate in the region of exponential growth; thus, the higher initial amplitude leads to a larger maximum amplitude at the saturation location for the OLES case. Consequently, when

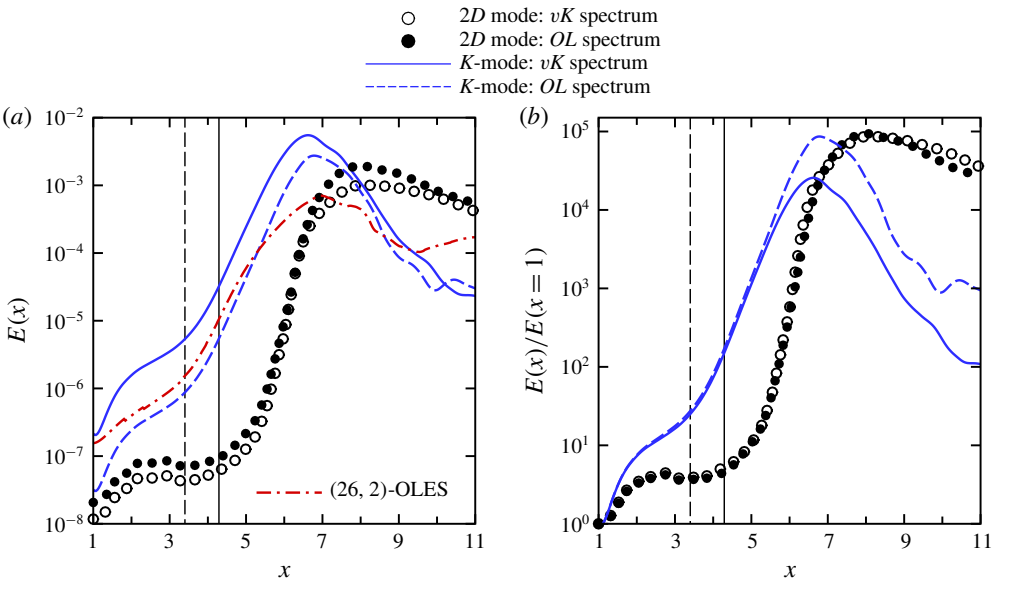

FIGURE 33. (Colour online) Streamwise development of disturbance kinetic energy for different FST energy spectra: (*a*) not-normalized, (*b*) normalized with inflow values. Plotted are 2D modes at the fundamental frequency and Klebanoff modes, mode (26, 5). Included in (*a*) is the streamwise evolution of mode (26, 2) as obtained from DNS with the OLES (dot-dashed curve). Onset of APG and separation location are indicated by vertical dashed lines and solid lines, respectively.

the local energy is normalized by the inflow value, the two curves collapse, indicating that the large initial amplitude is carried all the way in the downstream direction as indicated in figure 33(*b*). The opposite behaviour is observed for the K-mode, where the initial and maximum amplitudes are the largest for the case with the vKES. While both cases undergo the same transient growth, the exponential growth rate is slightly larger for the OLES case. As a result, the normalized energy curves are only identical for $x < 5$. Also, included in figure 33(*a*) is the streamwise evolution of low-frequency disturbance waves with the spanwise mode number identified in figure 32, mode (26, 2), which was obtained from the DNS with the OLES energy spectrum (dot-dashed curve). It is worth noting that, for the DNS with the OLES, $m = 2$ is the dominant mode until $x < 5.2$, from where onwards disturbance waves with $m = 5$ (K-modes) prevail further downstream and dominate the transition process similar to the DNS with the von Kármán energy spectrum.

Figure 34 compares the time- and spanwise-averaged skin-friction coefficients and displacement thicknesses obtained for the two cases, indicating that the separation region is slightly increased for the OLES case in both the streamwise and wall-normal directions. The transition process is governed mainly by the amplification of the K-mode for $Tu_0 = 2\,\%$. The K-mode is more energetic in the vKES case, and thus leads to a smaller separation bubble.

All results presented here were obtained for a fixed turbulent integral length scale $L_{11} = 1.5\delta_0$, where δ_0 is the boundary-layer thickness at the inflow boundary, while the FST intensity and spectrum content were varied. However, related studies of bypass transition on a zero-pressure-gradient flat-plate boundary layer have shown that the

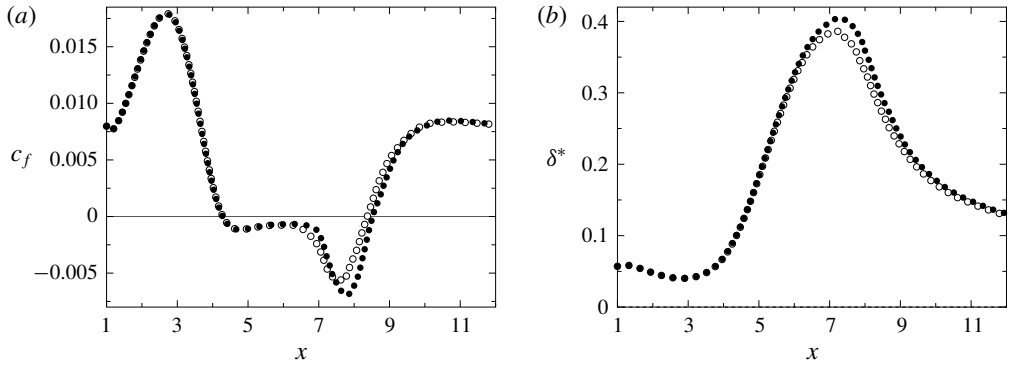

FIGURE 34. Time- and spanwise-averaged skin-friction coefficients (*a*) and displacement thickness (*b*) versus x: ○, von Kármán energy spectrum; ●, Ossia and Lesieur energy spectrum.

choice of the integral length scale, L_{11}, can have a significant effect on the transition process (Brandt *et al.* 2004). Therefore, simulations were carried out for $Tu_0 = 2.0\,\%$ using different integral length scales $L_{11} = 0.9\delta_0$, $1.5\delta_0$ and $3\delta_0$. These simulations have shown that, despite the considerable variation of the integral length scales, the size of the separation bubble was largely independent of L_{11} for the range investigated here. The same conclusion was obtained for the case with the lowest FST intensity $Tu = 0.1\,\%$. These results are not presented here since they did not display any particular new features/characteristics.

4. Conclusion

Highly resolved direct numerical simulations (DNS) were employed to investigate the effect of free-stream turbulence (FST) on the structure and dynamics of laminar separation bubbles (LSBs). Laminar separation on a flat plate was induced by a streamwise pressure gradient. A blowing–suction wall-normal velocity at the free-stream boundary of the computational domain was prescribed such that the resulting downstream pressure gradient closely matches that of accompanying water-tunnel experiments carried out in the Hydrodynamics Laboratory at the University of Arizona. Isotropic turbulence velocity fluctuations, which are obtained based on a weighted superposition of the continuous modes of the Orr–Sommerfeld and Squire equations, were seeded at the inflow boundary of the computational domain. Five different levels of FST intensity were considered, $Tu_0 = 0.1\,\%$, $0.5\,\%$, $1\,\%$, $2\,\%$ and $3\,\%$, in addition to the zero FST, which is used for comparison. This range of FST levels covers the typical conditions encountered from free flight to turbomachinery applications.

Based on the results presented here, corroborated by instantaneous flow visualizations, spectral analysis and modal decompositions, the transition process in LSB subjected to FST can be summarized as follows. The transition process in the LSB is caused by the strong amplification of high-frequency disturbances due to an inviscid Kelvin–Helmholtz (KH) instability of the separated shear layer and the low-frequency, 3D disturbances (Klebanoff mode). For the lowest level of FST, $Tu_0 = 0.1\,\%$, the inviscid KH instability is the dominant mechanism, while for moderate turbulent intensities, $Tu_0 \sim 0.5\,\%$–$1\,\%$, the disturbances resulting from both

the KH instability and the Klebanoff (K) modes (that are caused by FST) are blended together and contribute simultaneously to the transition process. For the elevated FST intensity, $Tu_0 = 2\,\%$–$3\,\%$, the transition mechanism is dominated by the presence of large-amplitude K-modes.

Results from a linear instability investigation based on the linearized Navier–Stokes equations (without additional assumptions as required by the linear stability theory) and the comparison with DNS results, indicated that the slow (algebraic) growth of the K-mode is followed by a strong exponential amplification downstream of the onset of the adverse pressure gradient. While 2D instability waves also exhibit exponential growth, the 2D disturbance waves can be distinguished from the K-mode by their exponential growth, i.e. by the larger growth rates for 2D modes. The combined effect of these two instability mechanisms, KH and K-mode, is that, for increased levels of FST, transition is accelerated, leading to a smaller mean separated region.

Detailed investigations were carried out to evaluate the effect of the FST energy spectrum used in the FST model. The general finding was that the energy spectrum of FST fluctuations has appreciable but limited effects on the prevalent separation and transition mechanisms for the cases investigated here; in particular, the bubble size was only mildly affected.

Acknowledgements

This work was supported by the Air Force Office of Scientific Research (AFOSR) under grant number FA9550-14-1-0184, with Dr D. R. Smith serving as the program manager.

REFERENCES

ABU-GHANNAM, B. J. & SHAW, R. 1980 Natural transition of boundary layers the effects of turbulence, pressure gradient, and flow history. *J. Mech. Engng Sci.* **22** (5), 213–228.

ALAM, M. & SANDHAM, N. D. 2000 Direct numerical simulation of 'short' laminar separation bubbles with turbulent reattachment. *J. Fluid Mech.* **410**, 1–28.

BALZER, W. & FASEL, H. F. 2016 Numerical investigation of the role of free-stream turbulence in boundary-layer separation. *J. Fluid Mech.* **801**, 289–321.

BOIKO, A. V., GREK, G. R., DOVGAL, A. V. & KOZLOV, V. V. 2002 *The Origin of Turbulence in Near-wall Flows*, 1st edn. Springer.

BRANDT, L., SCHLATTER, P. & HENNINGSON, D. S. 2004 Transition in boundary layers subject to free-stream turbulence. *J. Fluid Mech.* **517**, 167–198.

BRINKERHOFF, J. R. & YARAS, M. I. 2015 Numerical investigation of transition in a boundary layer subjected to favourable and adverse streamwise pressure gradients and elevated free stream turbulence. *J. Fluid Mech.* **781**, 52–86.

BURGMANN, S. & SCHRÖDER, W. 2008 Investigation of the vortex induced unsteadiness of a separation bubble via time-resolved and scanning PIV measurements. *Exp. Fluids* **45**, 675–691.

CHETAN, S. J. & FASEL, H. F. 2012 Experimental investigation of the structure and dynamics of laminar separation bubbles. In *50th AIAA Aerospace Sciences Meeting including the New Horizons Forum and Aerospace Exposition, AIAA Paper* 2012-755. American Institute of Aeronautics and Astronautics (AIAA).

DIWAN, S. S., CHETAN, S. J. & RAMESH, O. N. 2006 On the bursting criterion for laminar separation bubbles. In *IUTAM Symposium on Laminar–Turbulent Transition*, pp. 401–407. Springer.

DIWAN, S. S. & RAMESH, O. N. 2009 On the origin of the inflectional instability of a laminar separation bubble. *J. Fluid Mech.* **629**, 263–298.

DOVGAL, A. V., KOZLOV, V. V. & MICHALKE, A. 1994 Laminar boundary layer separation: instability and associated phenomena. *Prog. Aerosp. Sci.* **30** (1), 61–94.

EMBACHER, M. & FASEL, H. F. 2014 Direct numerical simulations of laminar separation bubbles: investigation of absolute instability and active flow control of transition to turbulence. *J. Fluid Mech.* **747**, 141–185.

FASEL, H. F. 2002 Numerical investigation of the interaction of the Klebanoff-mode with a Tollmien–Schlichting wave. *J. Fluid Mech.* **450**, 1–33.

GASTER, M. 1969 The structure and behaviour of laminar separation bubbles. *ARC Reports and Memoranda* 3595. Aeronautical Research Council (ARC).

GASTER, M. & GRANT, I. 1975 An experimental investigation of the formation and development of a wave packet in a laminar boundary layer. *Proc. R. Soc. Lond.* A **347** (1649), 253–269.

GOLDSTEIN, M. E. 2014 Effect of free-stream turbulence on boundary layer transition. *Phil. Trans. R. Soc. Lond.* A **372** (2020), 1–18.

GREENBLATT, D. & WYGNANSKI, I. J. 2000 The control of flow separation by periodic excitation. *Prog. Aerosp. Sci.* **36** (7), 487–545.

GROSCH, C. E. & SALWEN, H. 1978 The continuous spectrum of the Orr–Sommerfeld equation. Part 1. The spectrum and the eigenfunctions. *J. Fluid Mech.* **87** (1), 33–54.

HÄGGMARK, C. 2000 Investigations of disturbances developing in a laminar separation bubble flow. PhD thesis, KTH, Department of Mechanics, Stockholm.

HAMMOND, D. A. & REDEKOPP, L. G. 1998 Local and global instability properties of separation bubbles. *Eur. J. Mech. (*B*/Fluids)* **17** (2), 145–164.

HORTON, H. P. 1968 Laminar separation in two and three-dimensional incompressible flow. PhD thesis, University of London.

HOSSEINVERDI, S., BALZER, W. & FASEL, H. F. 2012 Direct numerical simulations of the effect of free-stream turbulence on 'long' laminar separation bubbles. In *42nd AIAA Fluid Dynamics Conference and Exhibit, AIAA Paper* 2012-2972. American Institute of Aeronautics and Astronautics (AIAA).

HOSSEINVERDI, S. & FASEL, H. F. 2013*a* Direct numerical simulations of transition to turbulence in two-dimensional laminar separation bubbles. In *51st AIAA Aerospace Sciences Meeting including the New Horizons Forum and Aerospace Exposition, AIAA Paper* 2013-264. American Institute of Aeronautics and Astronautics (AIAA).

HOSSEINVERDI, S. & FASEL, H. F. 2013*b* Numerical investigation of the effect of free-stream turbulence on separation control by pulsed vortex generator jets. In *43rd Fluid Dynamics Conference, AIAA Paper* 2013-2614. American Institute of Aeronautics and Astronautics (AIAA).

HOSSEINVERDI, S. & FASEL, H. F. 2016 Direct numerical simulations of laminar-to-turbulent transition in laminar separation bubbles in three-dimensional boundary-layer. In *46th AIAA Fluid Dynamics Conference, AIAA Paper* 2016-3793. American Institute of Aeronautics and Astronautics (AIAA).

HOSSEINVERDI, S. & FASEL, H. F. 2018 Role of Klebanoff modes in active flow control of separation: direct numerical simulations. *J. Fluid Mech.* **850**, 954–983.

HUERRE, P. & MONKEWITZ, P. A. 1990 Local and global instabilities in spatially developing flows. *Annu. Rev. Fluid Mech.* **22** (1), 473–537.

HUNT, J. C. R., DURBIN, P. A., KEVLAHAN, N. K. R. & FERNANDO, H. J. S. 1996 Non-local effects of shear in turbulent flows. In *Sixth European Turbulence Conference, Lausanne, Switzerland*, Springer.

JACOBS, R. G. & DURBIN, P. A. 1998 Shear sheltering and the continuous spectrum of the Orr–Sommerfeld equation. *Phys. Fluids* **10** (8), 2006–2011.

JACOBS, R. G. & DURBIN, P. A. 2001 Simulations of bypass transition. *J. Fluid Mech.* **428**, 185–212.

JEONG, J. & HUSSAIN, F. 1995 On the identification of a vortex. *J. Fluid Mech.* **285**, 69–94.

JONES, L. E., SANDBERG, R. D. & SANDHAM, N. D. 2008 Direct numerical simulations of forced and unforced separation bubbles on an airfoil at incidence. *J. Fluid Mech.* **602**, 175–207.

KENDALL, J. M. 1985 Experimental study of disturbances produced in a pretransitional laminar boundary layer by weak freestream turbulence. In *18th Fluid Dynamics and Plasma Dynamics*

and Lasers Conference, AIAA Paper 1985-1695. American Institute of Aeronautics and Astronautics (AIAA).

KENDALL, J. M. 1990 Boundary layer receptivity to freestream turbulence. In *21st Fluid Dynamics, Plasma Dynamics and Lasers Conference, AIAA Paper 1990-1504* American Institute of Aeronautics and Astronautics (AIAA).

KLEBANOFF, P. S. 1971 Effect of free-stream turbulence on a laminar boundary layer. *Bull. Am. Phys. Soc.* **16** (11), 1323.

KLEBANOFF, P. S. & TIDSTROM, K. D. 1959 Evolution of amplified waves leading to transition in a boundary layer with zero pressure gradient. *Tech. Note* D-195. NASA.

LANDAHL, M. T. 1975 Wave breakdown and turbulence. *SIAM J. Appl. Maths* **28** (4), 735–756.

LARDEAU, S., LESCHZINER, M. & ZAKI, T. 2012 Large eddy simulation of transitional separated flow over a flat plate and a compressor blade. *Flow Turbul. Combust.* **88** (1), 19–44.

LEIB, S. J., WUNDROW, D. W. & GOLDSTEIN, M. E. 1999 Effect of free-stream turbulence and other vortical disturbances on a laminar boundary layer. *J. Fluid Mech.* **380**, 169–203.

LUMLEY, J. L. 1967 The structure of inhomogeneous turbulent flows. In *Atmospheric Turbulence and Radio Wave Propagation* (ed. A. M. Yaglom & V. I. Tatarsky), pp. 166–178. Nauka.

MARXEN, O. & HENNINGSON, D. S. 2011 The effect of small-amplitude convective disturbances on the size and bursting of a laminar separation bubble. *J. Fluid Mech.* **671**, 1–33.

MARXEN, O., LANG, M., RIST, U., LEVIN, O. & HENNINGSON, D. S. 2009 Mechanisms for spatial steady three-dimensional disturbance growth in a non-parallel and separating boundary layer. *J. Fluid Mech.* **634**, 165–189.

MARXEN, O., LANG, M., RIST, U. & WAGNER, S. 2003 A combined experimental/numerical study of unsteady phenomena in a laminar separation bubble. *Flow Turbul. Combust.* **71** (1), 133–146.

MARXEN, O., RIST, U. & WAGNER, S. 2004 Effect of spanwise-modulated disturbances on transition in a separated boundary layer. *AIAA J.* **42** (5), 937–944.

MATSUBARA, M. & ALFREDSSON, P. H. 2001 Disturbance growth in boundary layers subjected to free-stream turbulence. *J. Fluid Mech.* **430**, 149–168.

MCAULIFFE, B. R. & YARAS, M. I. 2010 Transition mechanisms in separation bubbles under low-and elevated-freestream turbulence. *Trans. ASME J. Turbomach.* **132** (1), 11004–11010.

MEITZ, H. L. & FASEL, H. F. 2000 A compact-difference scheme for the Navier–Stokes equations in vorticity–velocity formulation. *J. Comput. Phys.* **157** (1), 371–403.

MICHELIS, T., YARUSEVYCH, S. & KOTSONIS, M. 2017 Response of a laminar separation bubble to impulsive forcing. *J. Fluid Mech.* **820**, 633–666.

MORKOVIN, M. V. 1969 On the many faces of transition. In *Viscous Drag Reduction* (ed. C. Sinclair Wells), pp. 1–31. Springer.

MOSER, R. D. & MOIN, P. 1987 The effects of curvature in wall-bounded turbulent flows. *J. Fluid Mech.* **175**, 479–510.

NA, Y. & MOIN, P. 1998 Direct numerical simulation of a separated turbulent boundary layer. *J. Fluid Mech.* **370**, 175–201.

OLSON, D. A., KATZ, A. W., NAGUIB, A. M., KOOCHESFAHANI, M. M., RIZZETTA, D. P. & VISBAL, M. R. 2013 On the challenges in experimental characterization of flow separation over airfoils at low Reynolds number. *Exp. Fluids* **54** (2), 1470.

OSSIA, S. & LESIEUR, M. 2001 Large-scale energy and pressure dynamics in decaying 2D incompressible isotropic turbulence. *J. Turbul.* **2** (13), 1–34.

OWEN, P. R. & KLANFER, L. 1953 On the laminar boundary layer separation from the leading edge of a thin aerofoil. ARC C.P. 220. Aeronautical Research Council (ARC).

POPE, S. B. 2001 *Turbulent Flows*. Cambridge University Press.

POSTL, D., BALZER, W. & FASEL, H. F. 2011 Control of laminar separation using pulsed vortex generator jets: direct numerical simulations. *J. Fluid Mech.* **676**, 81–109.

RADI, A. & FASEL, H. F. 2010 Experimental investigation of laminar separation bubbles on a flat plate. In *40th Fluid Dynamics Conference and Exhibit, AIAA Paper* 2010-4482. American Institute of Aeronautics and Astronautics (AIAA).

RAO, V. N., TUCKER, P. G., JEFFERSON-LOVEDAY, R. J. & COULL, J. D. 2013 Large eddy simulations in low-pressure turbines: effect of wakes at elevated free-stream turbulence. *Intl J. Heat Fluid Flow* **43**, 85–95.

RIST, U. 2003 Instability and transition mechanisms in laminar separation bubbles. In *VKI/RTO-LS Low Reynolds Number Aerodynamics on Aircraft Including Applications in Emerging UAV Technology*, pp. 1–29. von Karman Institute.

RIST, U. & MAUCHER, U. 2002 Investigations of time-growing instabilities in laminar separation bubbles. *Eur. J. Mech. (*B*/Fluids)* **21** (5), 495–509.

RODRÍGUEZ, D., GENNARO, E. M. & JUNIPER, M. P. 2013 The two classes of primary modal instability in laminar separation bubbles. *J. Fluid Mech.* **734**, R4.

RODRÍGUEZ, D. & THEOFILIS, V. 2010 Structural changes of laminar separation bubbles induced by global linear instability. *J. Fluid Mech.* **655**, 280–305.

SATTA, F., SIMONI, D., UBALDI, M., ZUNINO, P., BERTINI, F. & SPANO, E. 2007 Velocity and turbulence measurements in a separating boundary layer with and without passive flow control. *IMechE* A*: J. Power Energy* **221** (6), 815–818.

SCHMID, P. J. 2010 Dynamic mode decomposition of numerical and experimental data. *J. Fluid Mech.* **656**, 5–28.

SCHUBAUER, G. B. & SKRAMSTAD, H. K. 1948 Laminar-boundary-layer oscillations and transition on a flat plate. *NACA Tech. Rep.* 909. National Advisory Committee for Aeronautics.

SIMONI, D., LENGANI, D., UBALDI, M., ZUNINO, P. & DELLACASAGRANDE, M. 2017 Inspection of the dynamic properties of laminar separation bubbles: free-stream turbulence intensity effects for different Reynolds numbers. *Exp. Fluids* **58** (66), 1–14.

SIMONI, D., UBALDI, M. & ZUNINO, P. 2014 Experimental investigation of flow instabilities in a laminar separation bubble. *J. Therm. Sci.* **23** (3), 203–214.

SIROVICH, L. 1987 Turbulence and the dynamics of coherent structures. I. Coherent structures. *Q. Appl. Maths* **45** (3), 561–571.

SPALART, P. R. & STRELETS, M. K. 2000 Mechanisms of transition and heat transfer in a separation bubble. *J. Fluid Mech.* **403**, 329–349.

VON TERZI, D. A. 2004 Numerical investigation of transitional and turbulent backward-facing step flows. PhD thesis, The University of Arizona.

WATMUFF, J. H. 1999 Evolution of a wave packet into vortex loops in a laminar separation bubble. *J. Fluid Mech.* **397**, 119–169.

WESTIN, K. J. A., BOIKO, A. V., KLINGMANN, B. G. B., KOZLOV, V. V. & ALFREDSSON, P. H. 1994 Experiments in a boundary layer subjected to free stream turbulence. Part 1. Boundary layer structure and receptivity. *J. Fluid Mech.* **281**, 193–218.

WISSINK, J. G. & RODI, W. 2006 Direct numerical simulations of transitional flow in turbomachinery. *Trans. ASME J. Turbomach.* **128** (4), 668–678.

YARUSEVYCH, S., KAWALL, J. G. & SULLIVAN, P. E. 2006 Airfoil performance at low Reynolds numbers in the presence of periodic disturbances. *J. Fluids Engng* **128** (3), 587–595.

ZAKI, T. A. & DURBIN, P. A. 2006 Continuous mode transition and the effects of pressure gradient. *J. Fluid Mech.* **563**, 357–388.

ZAKI, T. A., WISSINK, J. G., RODI, W. & DURBIN, P. A. 2010 Direct numerical simulations of transition in a compressor cascade: the influence of free-stream turbulence. *J. Fluid Mech.* **665**, 57–98.